A&A, 712, A80 (2026)
https://doi.org/10.1051/0004-6361/202557419
© The Authors 2026

Astronomy & Astrophysics

BlackTHUNDER: Evidence of three massive black holes in a $z \sim 5$ galaxy

Hannah Übler[1,⋆], Giovanni Mazzolari[1], Roberto Maiolino[2,3,4], Francesco D'Eugenio[2,3], Nazanin Davari[5], Ignas Juodžbalis[2,3], Michele Perna[6], Jorryt Matthee[7], Raffaella Schneider[8], Rosa Valiante[5], Santiago Arribas[6], Elena Bertola[9], Andrew J. Bunker[10], Volker Bromm[11], Stefano Carniani[12], Stéphane Charlot[13], Giovanni Cresci[9], Mirko Curti[14], Richard Davies[1], Frank Eisenhauer[1,15], Andrew Fabian[16], Natascha M. Förster Schreiber[1], Reinhard Genzel[1,17], Kohei Inayoshi[18], Lucy R. Ivey[2,3], Gareth C. Jones[2,3], Boyuan Liu[19], Dieter Lutz[1], Daichi Kashino[20], Ruari Mackenzie[21,22], Eleonora Parlanti[12], Brant Robertson[23], Bruno Rodríguez del Pino[6], T. Taro Shimizu[1], Debora Sijacki[2,16], Eckhard Sturm[1], Sandro Tacchella[2,3], Linda Tacconi[1], Giulia Tozzi[1], Alessandro Trinca[24,5], Giacomo Venturi[12], Marta Volonteri[13], Chris Willott[25], and Saiyang Zhang[26,27]

(Affiliations can be found after the references)

Received 25 September 2025 / Accepted 4 May 2026

ABSTRACT

We present observational evidence of three massive, accreting black holes in the $z = 5.0167$ galaxy J0148-4214 from JWST/NIRSpec-IFU spectroscopy. The black holes are revealed through broad Hα emission (FWHM = 430–2920 km/s) without a forbidden-line counterpart in the bright [O III] doublet. Channel maps of the asymmetric central Hα profile isolate two spatially distinct broad-line regions (BLRs), separated by 190 ± 40 pc, while a third BLR is found in the galaxy outskirts with a projected separation of 1.7 kpc. We discuss whether this emission could be due to supernovae, shocks, winds, or massive stars, but find the BLR origin most likely. Using single-epoch virial relations, we estimated black hole masses of $\log(M_\bullet/M_\odot) = 7.9 \pm 0.4$ (primary), 5.8 ± 0.5 (secondary), and 6.3 ± 0.5 (third off-nuclear). We argue that the two central black holes will likely rapidly merge, with a simple dynamical friction time estimate of the order of $\lesssim$700 Myr. Assuming that the third off-nuclear black hole is also in the process of sinking towards the centre, it will likely lead to a second merger, and we investigated the detection probability of such mergers with LISA. Alternatively, the third black hole may be the result of a previous central three-body interaction or a gravitational recoil, where our observations would provide evidence that such black holes may retain their accretion discs and BLRs even in the aftermath of such extreme dynamical interactions. The possible discovery of a black hole triplet at high redshifts, together with other recent results on distant black hole pairs, indicates that multiple massive black hole systems were likely common in the early Universe. Our results highlight the importance of IFU observations for the detection of massive black hole multiplets in distant galaxies, the progenitors of massive black hole mergers that may be detected with next-generation gravitational wave observatories.

Key words. galaxies: active – galaxies: high-redshift – quasars: supermassive black holes

1. Introduction

There are essentially two ways of growing massive black holes following their formation: via gas accretion and through black hole mergers. The former is thought to be the dominant growth mode for the majority of massive black holes and across cosmic time (e.g. Soltan 1982; Volonteri et al. 2003; Sijacki et al. 2007). However, some models and simulations indicate that for certain black hole mass ranges and cosmic epochs, mergers could contribute significantly to massive black hole growth (e.g. Dubois et al. 2014; Kulier et al. 2015; Pacucci & Loeb 2020; Piana et al. 2021; Bhowmick et al. 2025).

Mergers of massive black holes have been predicted as a consequence of galaxy collisions (e.g. Begelman et al. 1980; Kauffmann & Haehnelt 2000; Menou et al. 2001; Volonteri et al. 2003; Di Matteo et al. 2005; Ferrarese & Ford 2005; Mayer et al. 2007; Khan et al. 2016; Rantala et al. 2017; Tremmel et al. 2017; Volonteri et al. 2020; Mannerkoski et al. 2022), and recent observations with JWST indeed confirm that the major merger rate at $z > 3$ is significant, on the order of 3−8 galaxies per Gyr, and even higher when accounting for minor mergers (e.g. Dalmasso et al. 2024; Puskás et al. 2025; Duan et al. 2025). Observationally, massive black hole pairs on sub-kiloparsec separations to separations of a few tens of kiloparsecs have been identified across a wide redshift range (e.g. Junkkarinen et al. 2001; Komossa et al. 2003; Comerford et al. 2009, 2013, 2015; Green et al. 2010; Husemann et al. 2018; Mannucci et al. 2022; Koss et al. 2023; Neureiter et al. 2023; Perna et al. 2023, 2025b; Scialpi et al. 2024; Übler et al. 2024b; Matsuoka et al. 2024; Zamora et al. 2025; Ulivi et al. 2025; see also Tanaka et al. 2024; Mérida et al. 2025), including some triplets in the nearby Universe (Deane et al. 2014; Liu et al. 2019; Pfeifle et al. 2019; Kollatschny et al. 2020). The identification of multi-black hole systems is aided by their emission signatures during an active galactic nucleus (AGN) phase. There is strong theoretical evidence that black holes also grow through enhanced gas accretion during the galaxy merging process (e.g. Kormendy & Gebhardt 2001; Di Matteo et al. 2005; Springel et al. 2005; Hopkins et al. 2008; Johansson et al. 2009; Van Wassenhove et al. 2012; Capelo et al. 2015; Liao et al. 2024; Blumenthal & Barnes 2018; Saeedzadeh et al. 2024; Talbot et al. 2024; but see also Steinborn et al. 2016).

During these phases of active growth, massive black holes can be detected through various spectral signatures, including the broad, permitted emission of gas rotating at high

⋆ Corresponding author: hannah@mpe.mpg.de

Open Access article, published by EDP Sciences, under the terms of the Creative Commons Attribution License (https://creativecommons.org/licenses/by/4.0), which permits unrestricted use, distribution, and reproduction in any medium, provided the original work is properly cited.
This article is published in open access under the Subscribe to Open model. Open access funding provided by Max Planck Society.

velocities (≥1000 km/s) around the black hole, forming the broad-line region (BLR); characteristic narrow-line ratios indicative of the hard ionizing radiation from an AGN; *X*-ray emission; or high-velocity (≥1000 km/s) outflows in both permitted and forbidden lines (e.g. Padovani et al. 2017, and references therein). Among these signatures, emission from the BLR is of particular interest because it allows a measurement of the black hole mass, assuming that the gas in the BLR is in virial equilibrium, or at least that its width and luminosity scale with black hole mass as calibrated locally (e.g. Kaspi et al. 2000; Greene & Ho 2005).

Broad-line regions of luminous quasars have been detected out to $z \sim 7$ and used to estimate black hole masses, mainly derived from Mg II$_{2796,2803}$ or C IV$_{1548,1551}$ (e.g. Willott et al. 2003, 2010; Jiang et al. 2007; Kurk et al. 2007; Trakhtenbrot et al. 2017). However, only in the last few years, BLR emission from bright hydrogen and helium lines has become accessible in $z \gtrsim 4$ AGNs and quasars, thanks to the spectroscopic capabilities of JWST in the infrared regime. Since then, a large number of high-z broad-line (Type I) AGNs have been discovered (e.g. Kocevski et al. 2023; Übler et al. 2023; Harikane et al. 2023; Greene et al. 2024; Kokorev et al. 2023; Matthee et al. 2024; Maiolino et al. 2024a; Furtak et al. 2024; Juodžbalis et al. 2026a; Taylor et al. 2025; Tripodi et al. 2025a). The detection of an off-centre broad Hβ line also allowed for the discovery of a close-separation massive black hole pair in a galaxy merger at $z = 7.15$, with a projected separation of the two nuclei of only 620 pc (Übler et al. 2024b). However, in this merger system the second black hole is a narrow-line (Type II) AGN, and only the mass of the off-centre black hole could be measured.

In this paper we present observations of the galaxy J0148-4214 at $z \sim 5.017$ obtained with the Integral Field Spectroscopy (IFS) mode of the Near-Infrared Spectrograph (NIRSpec) on board JWST (Jakobsen et al. 2022; Böker et al. 2022). We report the discovery of multiple broad Hα emission line regions in J0148-4214, providing evidence of three massive accreting black holes within 0.27″ (projected distance of 1.7 kpc). We describe the available data and processing of the NIRSpec-IFS data in Sect. 2. The discovery of multiple broad emission line regions and their possible interpretations are discussed in Sect. 3. Global mass estimates for J0148-4214 are described in Sect. 4. In Sect. 5 we discuss the properties of the black holes in J0148-4214, their relation to their host galaxy, and their likely fate. We conclude in Sect. 6.

Throughout this work, we adopt a Chabrier (2003) initial mass function (0.1−100 $M_\odot$) and a flat ΛCDM cosmology with $H_0 = 70\,\mathrm{km\,s^{-1}\,Mpc^{-1}}$, $\Omega_\Lambda = 0.7$, and $\Omega_m = 0.3$.

2. Observations and data processing

2.1. JWST/NIRCam data

J0148-4214 (RA 01:48:33.29, Dec +05:59:50.04; J2000) was observed as part of the EIGER GTO survey (PID: 1243; PI: S. Lilly) in JWST/NIRCam WFSS mode with the F356W filter (~3.1−4.0 μm; spectral resolution $R \sim 1600$) and simultaneous imaging in F115W, F200W, and F356W. The data reduction is described by Kashino et al. (2023). J0148-4214 was identified as a $z = 5.019$ Type I AGN by Matthee et al. (2024). Using the single-epoch calibration by Reines et al. (2013), they found a single black hole with mass $\log(M_\bullet/M_\odot)_{\mathrm{H}\alpha} = 7.32\pm0.10$ (excluding systematic uncertainties and dust correction) and bolometric luminosity $L_{\mathrm{bol}} = (5.9\pm0.4)\times10^{44}$ erg/s. The imaging data presented by Matthee et al. (2024) show a bright, slightly elongated red source and two small fainter and bluer sources within 0.5″ in projection. In the top left panel of Fig. 1 we show a 3″ × 3″ NIRCam false-colour composite of J0148-4214. F115W contours encompass the three distinct sources; faint emission to the north-west of the main target is also seen.

2.2. JWST/NIRSpec-IFU data

J0148-4214 was subsequently observed in JWST/NIRSpec-IFU mode as part of the BlackTHUNDER survey (PID: 5015; PIs: H. Übler, R. Maiolino). The NIRSpec data were taken on December 15, 2024, with a medium cycling pattern of eight dither positions and a total integration time of about 1 h with the high-resolution grating/filter pair G395H/F290LP, covering the wavelength range 2.87−5.14 μm ($R \sim 2000$−3500), and about 0.5 h with PRISM/CLEAR ($\lambda = 0.6$−5.3 μm; $R \sim 30$−300).

Raw data files were downloaded from the Barbara A. Mikulski Archive for Space Telescopes (MAST) and subsequently processed with the JWST Science Calibration pipeline[1] version 1.15.0 under the Calibration Reference Data System (CRDS) context jwst_1293.pmap. We made several modifications to the default reduction steps to increase data quality, which are described in detail by Perna et al. (2023) and which we briefly summarise here. Count-rate frames were corrected for $1/f$ noise through a polynomial fit. During calibration in Stage 2, we removed regions affected by failed open MSA shutters, cosmic rays and bad pixels. Remaining outliers were flagged in individual exposures following D'Eugenio et al. (2024); we rejected the 98$^{\mathrm{th}}$ (99.5$^{\mathrm{th}}$) percentile of the resulting distribution in the grating (prism) observations. The final cubes were combined using the 'drizzle' method with a pixel scale of 0.05″.

No target acquisition was included in our NIRSpec observing setup. To correct for the resulting astrometric inaccuracies, we use the NIRSpec-IFS prism data to construct pseudo images matching the available NIRCam data. Registering our pseudo images to the NIRCam images (which are in turn registered to *Gaia* Data release 2; Gaia Collaboration 2018; see Kashino et al. 2023), we find an average offset of about 0.21″. This is comparable to offsets found for other NIRSpec-IFS cubes (e.g. Arribas et al. 2024; Jones et al. 2024, 2026a; Lamperti et al. 2024; Übler et al. 2024a; Parlanti et al. 2025a).

We use spaxels away from the central source and free of line emission to perform a background subtraction. To obtain realistic flux uncertainties, for each spectral extraction performed during our analysis, we scale the formal error extension of the final data cube to match the rms in regions free of spectral features (see Übler et al. 2023). From simultaneous fitting of multiple emission lines in the NIRSpec-IFS high-resolution data, we measure a spectroscopic redshift of $z = 5.01672 \pm 0.00002$ for J0148-4214.

3. Discovery of multiple broad emission line regions

The high-resolution cube of J0148-4214 shows several strong rest-frame optical emission lines: Hβ, [O III]$_{4959,5007}$, [O I]$_{6300}$, Hα and [N II]$_{6548,6583}$ ([S II]$_{6717,6731}$ is seen but falls partly into the detector gap and is very noisy). In the bottom left panel of Fig. 1 we show a line map integrated in the wavelength range 3.9-4.0 μm, covering Hα and any [N II] emission, zoomed in on the position of J0148-4214. The cyan contours derived from the NIRCam F115W image are the same as in the top left panel. We show the approximate point-spread function (PSF) FWHM at the wavelength of Hα, which is ~0.197″, as a white circle (see Jones et al. 2026b). We indicate two extraction regions in

[1] https://jwst-pipeline.readthedocs.io/en/stable/

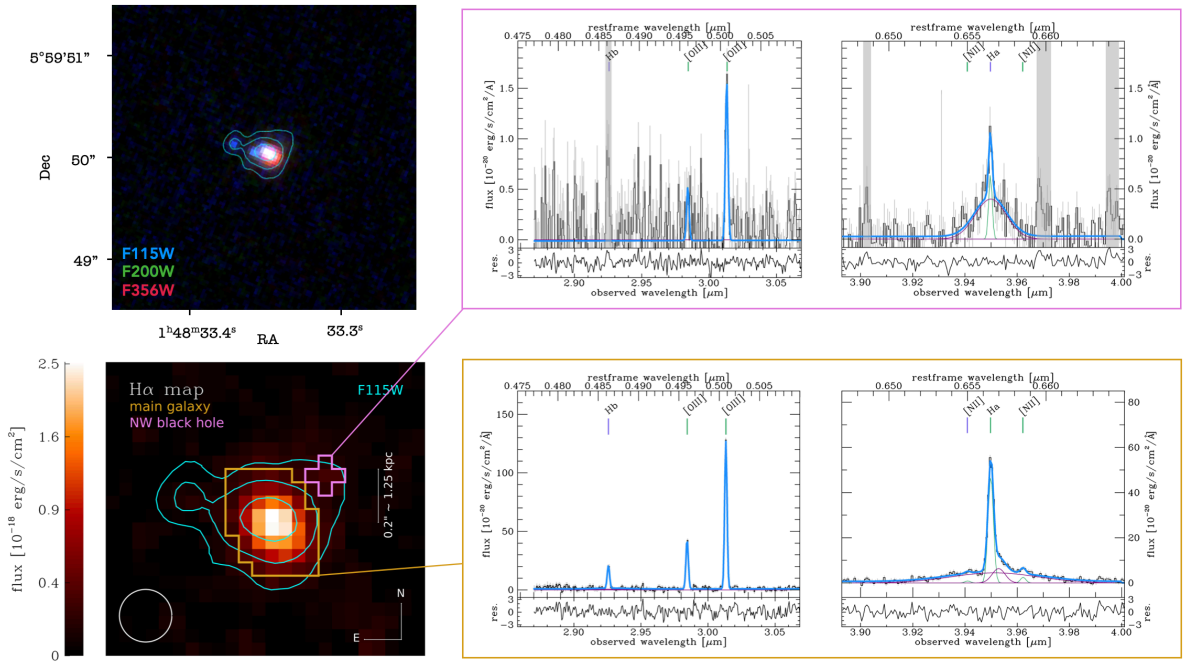

Fig. 1. *Top left*: RGB NIRCam image of J0148-4214 (see also Matthee et al. 2024). The blue contours are drawn at 0.009, 0.021, and 0.057 MJy/sr on the F115W image. The outermost contour encompasses the main target, the two smaller blue sources, and faint emission to the north-west of J0148-4214, where we locate a Type I AGN (see Sect. 3.1). The cutout size is 3″ × 3″. *Bottom left*: Hα line map integrated in the observed wavelength range λ = 3.9−4.0 µm. The white circle shows the approximate PSF FWHM at the wavelength of Hα. The cyan contours are the same as in the upper panel. Spectra extracted from the regions outlined in pink (NW black hole) and orange (main galaxy) are shown in the top and bottom right panels, respectively. We mark several artefacts with grey shading. Fits to the spectra are shown in blue, while the narrow and broad components are shown in green and purple, respectively. Residuals are plotted as (data-model)/error. While the permitted [O III] lines show no evidence of a broad component in the emission lines profile, Hα displays a complex profile for the main galaxy (bottom right panel), requiring two separate broad components (FWHM of 2920 ± 140 and 430 ± 80 km/s). In Sect. 3.1 we argue that this profile indicates the presence of two AGNs in the main galaxy. The broad Hα profile seen to the north-west of the main galaxy indicates the presence of a third AGN (*top right*).

orange and pink. The orange region includes emission from the main target; the extraction aperture is slightly stretched along the NE-SW direction, following the shape of the Hα emission. We note that this is also the orientation of the slicers in our NIRSpec-IFS observations, and the PSF may be elongated in slicer direction (see D'Eugenio et al. 2024). The corresponding integrated spectra around [O III]+Hβ and Hα+[N II] are shown in the bottom right panels. We show the full, high-resolution spectrum extracted from the main galaxy aperture in Appendix A. The Hα emission line exhibits a broad, asymmetric profile, possibly due to a superposition of two broad components. No corresponding broad emission is seen at the wavelength position of the brighter $[O\,III]_{5007}$ line. In the top right panels we show the integrated spectra extracted from the pink region[2], offset by about 0.27″(1.7 kpc) from the main source. Another broad component symmetric around Hα is clearly detected. Again, no corresponding broad component is detected in $[O\,III]_{5007}$. We perform a systematic search for additional broad Hα lines around the main galaxy aperture, using the pink extraction region as a template. While narrow $[O\,III]_{5007}$ and at lower significance narrow Hα are detected for all test apertures, we find no evidence of further broad Hα components.

In the following paragraphs, we discuss different physical scenarios that could give rise to the broad Hα components detected in J0148-4214. We begin with our favoured interpretation, three accreting massive black holes, and discuss and discard various other scenarios.

[2] We note that the conclusions presented in this paper remain unchanged if we increase the diameter of the pink extraction region to 5 pixels (~1.3 × $FWHM_{PSF}$).

3.1. Broad-line regions from three massive black holes

Broad emission line profiles in permitted lines without a counterpart in forbidden lines are commonly interpreted as emission from the broad-line region of accreting massive black holes. In J0148-4214 we find evidence of three such BLRs. First, the broad Hα profile extracted from the north-western (pink) region and detached from the broad Hα emission in the centre is clearly distinct in shape to the central emission: it is less broad than the central broad Hα emission and symmetric around the narrow Hα component. The broad Hα component has no counterpart in forbidden lines, specifically not in the $[O\,III]_{4959,5007}$ doublet. Therefore, it is unlikely to be associated with high-velocity gas in the interstellar medium (see Sect. 3.2). Instead, we here interpret this emission as the BLR of a black hole located in the outskirts of J0148-4214. At this off-nuclear position, it may be classified as an offset AGN (Comerford & Greene 2014), either in the process of being accreted into the centre of J0148-4214, or possibly having been ejected in a previous multi-body interaction or through a recoil kick of a previous black hole merger (Peres 1962; Bekenstein 1973; Saslaw et al. 1974; Mikkola & Valtonen 1990; Volonteri et al. 2003; Madau & Quataert 2004; Merritt et al. 2004; Sijacki et al. 2011; Blecha et al. 2016; Mannerkoski et al. 2022; Partmann et al. 2024).

Second, the broad Hα emission extracted from the central region of J0148-4214 (orange region) is clearly asymmetric. Similar profiles have been found for two AGNs at z = 4−6 observed with NIRSpec-MSA in the JADES survey (Eisenstein et al. 2026) by Maiolino et al. (2024a), who interpreted them as signatures of two AGNs within the MSA slit

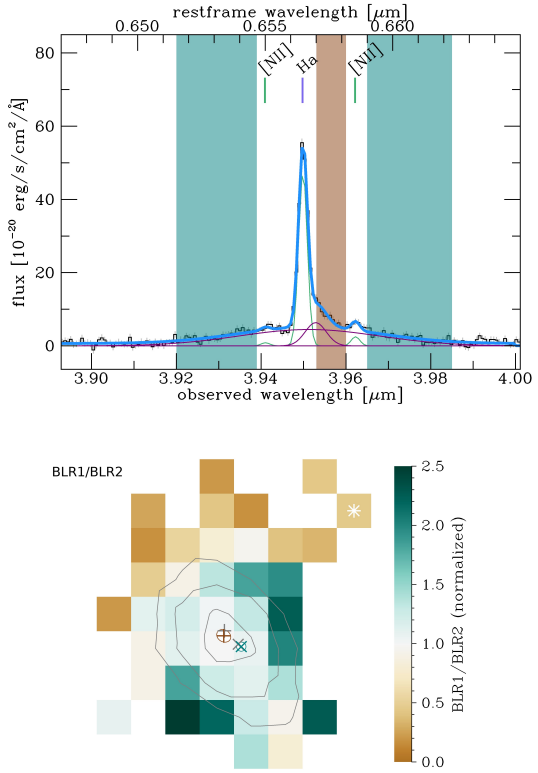

Fig. 2. *Top*: Illustration of the extraction regions for the BLR channel maps, as described in Sect. 3.1. The wavelength ranges to construct BLR1 and BLR2 are shown in teal and brown shading, respectively. We note that in this illustration, BLR2 is contaminated by BLR1, and we subtracted the contamination as described in the main text to obtain a clean channel map for BLR2. *Bottom*: Map of the ratio BLR1/BLR2 after normalisation to peak flux. We plot pixels with S/N $\geq$ 0.5 and draw contours at S/N = 3, 5, 8 for reference, where the S/N is calculated from the normalised ratio BLR1/BLR2. The teal cross and brown plus show the centroids of the channel maps for BLR1 and BLR2, with ellipses indicating two times the centroid uncertainty, derived as described in Sect. 3.1. As grey symbols we show the centroids derived from maps including only pixels with S/N $\geq$ 2 (uncertainties are omitted for clarity). The white star marks the position of the third BLR detected in J0148-4214. A modulation from the north-eastern region to the south-western region is visible, as expected for the images of two point sources spatially separated along that axis.

($\lesssim$0.2″) through double-Gaussian fits. Without further spatial information such an interpretation remains uncertain, because asymmetric BLRs can also be caused by an anisotropic gas distribution, inflows or outflows in the BLR, or a specific BLR geometry (e.g. Storchi-Bergmann et al. 2017, and references therein). However, if there are indeed two AGNs, the spatial information afforded through NIRSpec-IFS can help to separate their emission features (see Übler et al. 2024b). While we have no evidence of two central emission peaks in the Hα line map derived from our NIRSpec-IFS data, a visual inspection of the central region of J0148-4214 indeed suggests changes of the broad-line profile shape across the central spaxels.

For a quantitative investigation we employ a spectro-astrometric approach (e.g. Beckers 1982; Bailey 1998; Gnerucci et al. 2010) and constructed channel maps of the two putative BLRs. Here, it is important to avoid any narrow line emission from Hα or [N II]$_{6548,6583}$ which would contaminate the BLR light maps. Therefore, we proceed as follows: after subtraction of the (faint) continuum emission we derived a map of the broader BLR component (BLR1) by integrating emission at observed wavelengths $\lambda_{\rm obs}$ = 3.92–3.939 μm and $\lambda_{\rm obs}$ = 3.965–3.985 μm, i.e. omitting any narrow Hα and [N II]$_{6548,6583}$ emission from the host galaxy, as well as the putative second BLR component (see teal shading in the top panel of Fig. 2). Next, we derived a map of the narrower BLR component (BLR2), contaminated by BLR1, by integrating emission at observed wavelengths $\lambda_{\rm obs}$ = 3.953–3.96 μm (brown shading in top panel of Fig. 2), i.e. again omitting any narrow Hα and [N II]$_{6548,6583}$ emission from the host galaxy. We used our best fit to the central aperture spectrum (see below) to calculate the fractional contribution of flux from BLR1 to the total flux in this wavelength range with respect to the flux in our BLR1 map. We used the BLR1 map to subtract this fractional contribution from the contaminated BLR2 map, to obtain a clean map of BLR2. The resulting maps are shown in Fig. B.1. They have a distinct flux distribution, indicating that the asymmetric broad emission does not originate from a single point source. We determined the centroids of the two sources through two-dimensional Gaussian fits to the flux distributions of the two maps (see Appendix B for details on the precision). We used a box with half window size ~3.5 × FWHM$_{\rm PSF}$. Uncertainties are derived through Monte Carlo methods by varying the input images 10 000 times each with their associated noise, repeating the fits (see Appendix B). Then, we derived a projected spatial separation of $d_{\rm I,II}$ = 190 ± 40 pc between the centroids of BLR1 and BLR2 (~0.03″), where the uncertainty on the measurement calculated from the best-fit uncertainty is consistent with the uncertainty derived from the Monte Carlo runs. As an additional test, we measured the centroids including only pixels with S/N $\geq$ 2 (uncertainties are again derived through 10 000 Monte Carlo runs). The such derived centroids agree with our above measurements within the uncertainties. The corresponding projected spatial separation of BLR1 and BLR2 from this method is $d_{\rm I,II} = 160^{+40}_{-30}$ pc (~0.026″), consistent with our first measurement. In Appendix C we describe a mock test for the recovery of the distance between the BLRs from our channel maps. This gives consistent results ($d_{\rm I,II,mock} = 200^{+60}_{-40}$ pc), though indicates that the uncertainty associated with our distance measurement may be underestimated by 10–20 pc. We note that the offset we find is much larger than the BLR size associated with a single black hole (typically sub-parsec to ~ parsec scales; e.g. Kaspi et al. 2000; Bentz et al. 2013; GRAVITY Collaboration 2024; GRAVITY+ Collaboration 2026).

To further highlight the significance of the offset between the two BLRs, in the bottom panel of Fig. 2 we show the ratio of the two BLR maps (after normalisation to peak flux), which illustrates a NE-SW pattern, as expected from two images of two point sources that are spatially offset along that axis (see also Appendix C). We emphasise that we would not expect to see any of these signatures if the asymmetric broad Hα emission originated from a single source, i.e. a black hole with a peculiar BLR geometry, including absorption or asymmetric emission or velocity distribution within the BLR. We reiterate that typical BLR sizes are on $\lesssim$ parsec scales, i.e. at least 150 times smaller than the centroid separation we measure.

For further analysis, we performed a multi-component Gaussian fitting of the high-resolution spectra, assuming that the broad emission components stem from three massive, accreting black holes. We included a narrow Gaussian for Hβ, [O III]$_{4959,5007}$, [O I]$_{6300}$, Hα, [N II]$_{6548,6583}$. We do not fit [S II]$_{6717,6731}$ because the lines are close to the detector gap in a region of elevated noise. The intensity ratio of the [O III] doublet is fixed to [O III]$_{\lambda5007}$/[O III]$_{\lambda4959}$ = 2.98, as given by the Einstein coefficients of the two levels; similarly, the intensity

ratio of the [N II] doublet is fixed to $[\mathrm{N\,II}]_{\lambda6584}/[\mathrm{N\,II}]_{\lambda6548} = 2.94$ (e.g. Osterbrock & Ferland 2006). The narrow line emission is assumed to trace the interstellar medium in J0148-4214. We tied the line centroids and line widths separately for [O III]+Hβ and for Hα+[N II]. These groups of lines are close enough in wavelength to not expect significant differences in the instrument line-spread function (LSF; see Jakobsen et al. 2022). We also included a linear polynomial to account for any continuum emission. To model the BLRs in J0148-4214, we included two broad Gaussians for Hα and Hβ for the spectrum extracted from the central region (Fig. 1, orange aperture), and one broad Gaussian for the spectrum from the north-west (pink aperture). In both cases, the relative velocities and line widths are tied between Hα and Hβ. The best-fit emission line fluxes are listed in Table 1. We highlight that the integrated flux ratio of the two broad Hα components in the centre is about 0.2. This is different from results for double-Gaussian fits which have been performed for some high-z AGNs with symmetric broad components, which typically yield values around 0.5 and indicate a non-Gaussian shape of the BLR (D'Eugenio et al. 2026b,a). In general, non-Gaussian BLR shapes have been observed for a few high S/N, high-z AGNs (e.g. D'Eugenio et al. 2026a; Rusakov et al. 2026; Torralba et al. 2026) and more frequently for AGNs in the nearby Universe (e.g. Kollatschny & Zetzl 2011, 2013, and references therein; see also Ji et al. 2026). For the case of J0148-4214 the Gaussian decomposition provides an adequate fit to the data, as evidenced by the small and regular residuals (Fig. 1, right panels). However, it is possible that higher S/N or higher spectral resolution data could reveal deviations from Gaussian shapes. A systematic investigation of the BLR shapes and possible parametrisations for the full BlackTHUNDER sample will be presented in a forthcoming work.

We note the velocity offsets of the three broad components with respect to the central narrow Hα emission from our fits. For the primary broad Hα component and the secondary broad Hα component we find velocity offsets of $\Delta v = 110$ and $\Delta v = 228$ km/s, respectively, while the third, off-nuclear broad Hα component has a velocity offset of only $\Delta v = 3$ km/s (or $\Delta v = 10$ km/s with respect to the narrow Hα component at the off-nuclear position).

From our fiducial model, we find a narrow flux ratio $\mathrm{H}\alpha_\mathrm{n}/\mathrm{H}\beta_\mathrm{n} = 3.0 \pm 0.2$ for the main galaxy spectrum, potentially indicating a low attenuation of $A_V \sim 0.13$, using the attenuation law by Calzetti et al. (2000) or the extinction curve by Gordon et al. (2003), but also consistent with no dust attenuation under Case B recombination. For the BLR, values higher than the canonical Case B are routinely observed (e.g. Osterbrock 1977, 1981; Crenshaw et al. 1988; La Mura et al. 2007; Ilić et al. 2012). A broad component in Hβ corresponding to the primary AGN detected from the Hα emission is preferred by the fit, although it is only marginally detected. We find a flux ratio of $\mathrm{H}\alpha_\mathrm{BLR1}/\mathrm{H}\beta_\mathrm{BLR1} \sim 11$. If this ratio is (partly) due to reddening, instead of collisional excitation due to the much higher densities in the BLR, our black hole mass estimates (see Sect. 5.1) would correspond to lower limits. We followed a similar approach to fit the low-resolution prism observations, described in Appendix D.

For the high-resolution data, we also performed a spaxel-by-spaxel fitting for the main galaxy to constrain the narrow-line kinematics. To this end, we fixed the line centroids and widths of the BLR components to the best-fit values from the main galaxy aperture spectrum (Fig. 1), and otherwise proceeded as for our fiducial fit as described above. Resulting flux, velocity and velocity dispersion maps for $[\mathrm{O\,III}]_{5007}$ are shown in Appendix E.

Table 1. $R \sim 2700$ emission line fluxes.

	Main Galaxy
$\mathrm{H}\beta_\mathrm{n}$	4.28 ± 0.25
$\mathrm{H}\beta_\mathrm{BLR\ 1}$	1.69 ± 0.90
$[\mathrm{O\,III}]_{5007}$	28.33 ± 0.38
$[\mathrm{O\,I}]_{6300}$	0.59 ± 0.12
$\mathrm{H}\alpha_\mathrm{n}$	12.14 ± 0.59
$\mathrm{H}\alpha_\mathrm{BLR\ 1}$	18.27 ± 1.44
$\mathrm{H}\alpha_\mathrm{BLR\ 2}$	3.91 ± 0.86
$[\mathrm{N\,II}]_{6583}$	0.63 ± 0.14
	North-western region
$[\mathrm{O\,III}]_{5007}$	3.83 ± 0.70
$\mathrm{H}\alpha_\mathrm{n}$	1.07 ± 0.45
$\mathrm{H}\alpha_\mathrm{BLR\ 3}$	5.98 ± 1.41

Notes. Observed $R \sim 2700$ emission line fluxes in units of 10^{-18} erg/s/cm^2, extracted assuming our fiducial model: two central BLRs (orange aperture in Fig. 1; main galaxy) and one BLR in the north-western region (pink aperture in Fig. 1; NW black hole). We note that no second component is preferred by the fit for the much fainter broad Hβ emission in the centre, and also that the primary BLR component is only marginally detected in Hβ. For the north-western region, we do not report fluxes for Hβ because of an artefact at this line position; $[\mathrm{O\,I}]_{6300}$ and [N II] are not significantly detected.

3.2. A single black hole in the centre

We explore alternative interpretations of the broad Hα emission from the main galaxy aperture. In the discovery paper by Matthee et al. (2024) the authors consider a fit with a single BLR component for Hα (in addition to narrow Hα emission and broad [N II] emission) to their lower spectral resolution NIRCam grism data, estimating a (single) black hole mass of $\log(M_\bullet/M_\odot) = 7.32 \pm 0.10$. If we fit a single H$\alpha$ BLR component in addition to the narrow line emission to the main galaxy aperture spectrum, we find $\log(M_\bullet/M_\odot) = 7.69 \pm 0.42$, consistent within the uncertainties with the estimate by Matthee et al. (2024). Their somewhat lower black hole mass estimate can be explained through their choice of a broad [N II] component, while we include only a narrow line contribution for [N II], informed by the line profile of other forbidden emission lines, especially [O III], which was not available from the NIRCam grism observations. However, the asymmetric profile of the broad Hα component, which is more pronounced in our high-resolution data, is not well fit by a single Gaussian, and we therefore disregard this model.

However, there could be a single black hole with a non-Gaussian, asymmetric BLR shape, for instance due to strong inflows or outflows in the BLR (e.g. Rigamonti et al. 2025; Rosborough et al. 2025), or due to other anisotropic gas distributions. Asymmetric BLR shapes are known in AGNs in the local Universe, including in long-term monitoring campaigns (see e.g. Peterson et al. 2002; Lu et al. 2022 for galaxy NGC 5548; Fries et al. 2024). However, if the emission originates from within a single BLR (i.e. a point source for the cosmological distance of J0148-4214), we would have expected the same flux distribution from our mapping exercise of the two components of the broad Hα emission, which is not the case (see Sect. 3.1). Consequently, we conclude that the presence of two BLRs is a more likely scenario.

Another option could be a single BLR affected by a blue-shifted Hα absorber, a scenario that has been observed in several high- and low-z AGNs (e.g. Matthee et al. 2024; Juodžbalis et al. 2024a; D'Eugenio et al. 2026b,a; Ji et al. 2025,

2026; Loiacono et al. 2025; Lin et al. 2026b,a; Wang et al. 2024; Ma et al. 2026). To investigate this, we considered a model including possible absorption of the continuum and broad emission, modelled with a Gaussian velocity distribution, assuming a standard parametrisation of

$$f_{\rm abs} = 1 - C_f + C_f \cdot \exp\left\{-\tau_0 \cdot \exp\left[-0.5\left(c\frac{1-\lambda_{\rm abs}/\lambda}{\sigma_{\rm abs}}\right)^2\right]\right\},$$

where C_f is the covering factor of the absorber, τ_0 is the optical depth at the line centre, c is the speed of light, $\lambda_{\rm abs}$ is the centroid of the absorption, and $\sigma_{\rm abs}$ is the effective velocity dispersion of the absorbing gas (see Draine 2011; Juodžbalis et al. 2024a; D'Eugenio et al. 2026b,a; Ji et al. 2025; Loiacono et al. 2025).

To explore this scenario, due to the known parameter correlations in the absorption model (D'Eugenio et al. 2026a), we adopt a Bayesian framework following the methods outlined by D'Eugenio et al. (2026a). We modelled simultaneously the region around Hα, as well as adjacent spectral windows (including Hβ, [O III]$_{4959,5007}$, [O I]$_{6300}$, [N II]$_{6548,6583}$, [S II]$_{6717,6731}$). The narrow lines share the same redshift and velocity dispersion, which helps to constrain the redshift and dispersion of Hα in the presence of an absorber. We obtain a best fit with an absorber blue-shifted by 100 km/s, with $\sigma_{\rm abs} = 88 \pm 4$ km/s, $C_f = 0.996^{+0.003}_{-0.008}$, and $\tau_{0,{\rm H}\alpha} = 3.1^{+0.3}_{-0.2}$. For this model, the (single) central black hole has a mass of $\log(M_\bullet/M_\odot) = 7.6$, accreting at 20 per cent of its Eddington limit. These parameters are comparable to other results for little red dots (e.g. D'Eugenio et al. 2026b). However, absorption from the unstable $n = 2$ energy level requires extremely high column densities of neutral hydrogen and, effectively, extremely high densities, comparable to what is typically inferred for the BLR (e.g. Juodžbalis et al. 2024a). For this reason, it is generally thought that the hydrogen absorber should be located within or immediately outside the BLR, i.e. on sub-parsec scales. In this case, we can discard this model on the same grounds as the asymmetric single BLR model: we would expect no change of the centroid when sampling the BLR over different spectral windows. However, for completeness, we calculate ΔBIC for this model and the corresponding fiducial model of two central BLRs, and find that the latter is preferred with $\Delta{\rm BIC} \sim 30$.

Could we see a single BLR in combination with a redshifted outflow in the centre? Outflows in distant galaxies are more typically observed symmetric around the ISM emission or blue-shifted due to differential extinction, but red-shifted emission associated with outflows has also been reported (e.g. Carniani et al. 2024). Interestingly, the majority of the low- to moderate-luminosity AGNs discovered with JWST at $z \sim 4$–6 lack the strong outflow emission typically associated with more luminous quasars (e.g. Maiolino et al. 2024a). The broad component detected in Hα does not have a counterpart in the forbidden [O III] lines, which however feature a narrow component more than twice as bright as the narrow Hα component. We can therefore rule out an outflow origin of the secondary broad Hα component in the centre with metallicity and density similar to the galaxy ISM. However, the [O III] component of an outflow could be suppressed due to high densities. Assuming a gas phase metallicity of 0.1 solar or higher, we calculate a minimum density of $n_e > 10^6$ cm^{-3} to bring the non-detection of a broad [O III] component in line with the (secondary) broad Hα flux, based on calculations with `pyneb`. At this density, we estimate a gas mass of about 2000 solar masses from the (secondary) broad Hα flux, which should be unstable to gravitational collapse. Alternatively, the putative outflowing gas could have more typical ISM density, but would then require a metallicity significantly lower compared to the galaxy ISM. We therefore deem the outflow scenario highly unlikely.

3.3. Supernovae, shocks, winds, and massive stars

Core-collapse supernovae (CCSNe) produce broad Balmer emission lines, although those are typically characterised by much broader line profiles (several 1000 to 10 000 km/s; Taddia et al. 2013; Gutiérrez et al. 2017). These broad-line components are often blue-shifted or show P Cygni features, which is not the case for J0148-4214, neither in the centre nor in the outskirts. As discussed in detail by Maiolino et al. (2025), average individual SNe may reach broad Hα luminosities of 10^{41} erg/s (e.g. Pastorello et al. 2002; Taddia et al. 2013) or up to 10^{42} erg/s in extreme cases. For the AGN in J0148-4214, we measure broad Hα luminosities of $\log({\rm H}\alpha_{\rm BLR}/({\rm erg/s})) = 42.7 \pm 0.1$, 42.0 ± 0.1 and 41.2 ± 0.2, i.e. above the typical luminosity for individual SNe, though in reachable range for the two less luminous broad components.

For the two central AGNs we can leverage the existing NIRCam grism observations of J0148-4214 obtained on 14 January 2023 to compare the broad Hα luminosities over a time span of about 120 days rest-frame (23 month observed frame). If the central BLRs in J0148-4214 are indeed SNe initially observed at peak luminosity, over a course of about 120 days we may expect a drop in broad Hα luminosity of about a quarter to half an order of magnitude (although individual cases can vary; see Pastorello et al. 2002; Taddia et al. 2013). We re-fit the lower-resolution, one-dimensional spectrum by Matthee et al. (2024) with a two-BLR model and measure $\log({\rm H}\alpha_{\rm BLR}/({\rm erg/s})) = 42.6 \pm 0.1$ and 42.0 ± 0.5, i.e. consistent with the values derived from our NIRSpec-IFS data. We therefore deem the SN scenario for the two central broad Hα components unlikely.

Unfortunately, we cannot perform the same test for the NW broad Hα. Instead, we explore more generally whether the broad Hα emission at the NW location could be due to shocks. Specifically, we consider the shock models by Allen et al. (2008), as implemented in MAPPING V (Sutherland et al. 2018), with the following parameters: a pre-shock density of 1/cm^3, magnetic field strengths [0.0001–10] μG, and solar and SMC metallicity. Based on the line width of the broad Hα component, we assume a shock velocity of 1000 km/s (see Perna et al. 2020). The Hα luminosities predicted by these models (up to $\sim 1.7 \times 10^{40}$ erg/s) are lower compared to the broad NW Hα component. Furthermore, these models predict emission line ratios incompatible with what we observe. As an example, the predicted [O I]$_{6300}$/Hα ratio is $\gtrsim$0.3. We do not detect [O I]$_{6300}$ in the NW spectrum extracted from the pink aperture, and also from the main galaxy aperture we find [O I]$_{6300}$/H$\alpha \ll 0.3$ for any of the broad Hα components. We note that also other features typical of CCSN are not seen throughout J0148-4214, such as a broad emission bump around 4600 Å (Gal-Yam 2012).

Localised starburst and very massive stars can also produce broad Balmer lines. Could these explain the broad Hα in the off-nuclear region? Star-formation-driven winds in high-z galaxies have typical FWHM of $\sim$400–500 km/s (see e.g. Förster Schreiber et al. 2019; Carniani et al. 2024), while we find a broad Hα FWHM of >1000 km/s. More importantly, if the broad Hα would be due to outflows (star-formation-driven or AGN-driven), we would expect to see corresponding broad emission in [O III]$_{4959,5007}$ (e.g. Harrison et al. 2016; Concas et al. 2022; Cresci et al. 2023; Bertola et al. 2025; Venturi et al. 2026), which is not observed for J0148-4214. In the case of very mas-

sive stars, the associated equivalent widths of Hα fall typically below 20 Å after ∼10 Myr (Martins et al. 2020). For the Hα BLRs in J0148-4214 we find high equivalent widths of Hα ($\log(\mathrm{EW}_{\mathrm{H}\alpha}/\text{Å}) = 2.7 \pm 0.3, 2.0 \pm 0.3$ and 2.5 ± 1.2). Therefore, we deem also this scenario unlikely.

To summarise, considering various physical scenarios, we conclude that we find evidence of three distinct Type I AGNs in J0148-4214: two at close separation in the centre, and one in the outskirts of J0148-4214 in the north-west. In both regions we observe broad Hα emission without a counterpart in the forbidden lines, and spectral features typically associated with shocks or supernovae are absent. Specifically in the centre, we find evidence of two compact sources based on their distinct line maps through spectro-astrometry, coinciding with an asymmetric integrated line shape consistent with a superposition of two BLRs. For the reminder of this paper, we therefore proceed with the discussion of three massive, active black holes in J0148-4214.

4. Derivation of global galaxy properties

4.1. SED fitting

To constrain the global properties of J0148-4214, we performed a spectral energy distribution (SED) fitting analysis using `CIGALE` (Boquien et al. 2019). We leveraged the PRISM spectra to extract the photometry directly from the continuum emission. First, we masked any strong emission lines due to the uncertain contribution of the AGN. Then, we sampled the PRISM continuum in nine bins of 4000 Å, which provides a good representation of the continuum shape without being too sensitive to noise fluctuations.

The SED fitting was performed considering a large parameter grid and taking into account the AGN emission. We used delayed star formation history (SFH) models which are able to reproduce both early-type and late-type galaxies, with an additional term that allows for a recent, constant burst in star formation. We adopted stellar templates from Bruzual & Charlot (2003), and a Chabrier (2003) initial mass function. We considered two different metallicities for the stellar populations (solar and 0.2 solar) and a separation between the young and old stellar populations between 10 and 500 Myr. We also included the nebular emission module with gas phase metallicities of solar and 0.2 solar. This module was computed by `CIGALE` in a self-consistent manner using a grid of `Cloudy` photoionisation calculations (Ferland et al. 2013). For the attenuation of the stellar continuum emission, we used the `dustatt_modified_CF00` module (Charlot & Fall 2000), which allows different attenuations for the young and old stellar populations. We selected a narrow range of $A_{V,\mathrm{ISM}}$, the attenuation of the stellar continuum, to match the result obtained from the spectral analysis assuming $E(B-V)_{\mathrm{star}} = 0.44E(B-V)_{\mathrm{gas}}$. Assuming $E(B-V)_{\mathrm{star}} = E(B-V)_{\mathrm{gas}}$, as may be appropriate for young stellar populations (see Puglisi et al. 2016; Perna et al. 2025a), lowers our best estimate of the stellar mass by 0.1 dex. We also included dust emission in the infrared following Dale et al. (2014).

For the AGN contribution we employed the `skirtor2016` (Stalevski et al. 2016) module updated by Yang et al. (2020), which has demonstrated to be reliable in studying various aspects of AGNs (e.g. Mountrichas et al. 2022; López et al. 2023; Yang et al. 2023; Mazzolari et al. 2025). The SED produced by the AGN combines emission from the accretion disc, torus, and polar dust. The accretion disc, responsible for the UV-optical emission in the central region, is parametrised according to Schartmann et al. (2005). Photons from the accretion disc can be obscured and scattered by dust in the vicinity, within the torus and/or in the polar direction. For the torus, the `skirtor2016` module employs a clumpy two-phase model (Stalevski et al. 2016), based on the 3D radiative-transfer code SKIRT (Baes et al. 2011; Camps & Baes 2015). For the polar dust component, we used the Small Magellanic Cloud (SMC) extinction curve, recommended for AGN observations (e.g. Bongiorno et al. 2012). For the extinction amplitude, we chose a range up to $E(B-V) = 1.5$. The code assumes energy conservation for both the polar dust absorbing the AGN emission and for the ISM dust, the former contributing to the AGN mid-infrared emission, the latter re-emitting isotropically following the prescriptions of Dale et al. (2014). Finally, we allowed for inclination values from 20 to 90 degrees and varied the AGN fraction (defined as the ratio between the AGN luminosity and the total galaxy luminosity between 0.13 and 5 µm) from 0.1 (weak AGN contamination) to 0.9 (dominant AGN emission).

We obtain a stellar mass estimate of $\log(M_\star/M_\odot) = 9.1 \pm 0.5$, based on a circular aperture extraction with a diameter of 11 pixels ($r = 1.7$ kpc). This aperture includes the one of the two small blue sources closer to J0148-4214 seen in the NIRCam imaging. The position of AGN III is just at the boundary of the aperture. In Sect. 5.4 we discuss a separate stellar mass estimate for the NW black hole region.

4.2. Integrated velocity dispersion and dynamical mass

We measured the integrated ionised gas velocity dispersion from our fit to the narrow [O III] line emission from the main galaxy aperture spectrum (see Fig. 1), accounting for the LSF, and find $\sigma_{\mathrm{int,[OIII]}} = 63$ km/s, adopting a floor uncertainty of 5 km/s. Following Übler et al. (2023), we used the empirical relation between integrated velocity dispersion of ionised gas and stars found by Bezanson et al. (2018) to estimate the integrated stellar velocity dispersion $\sigma_\star$ for our target. We note that this conversion was established for $z \sim 1$ galaxies with stellar masses $\log(M_\star/M_\odot) \gtrsim 9.9$; and yet, no systematic investigation of this type exists for higher-z galaxies (for AGN-specific studies in the local Universe see Bennert et al. 2018; Remigio et al. 2025). For J0148-4214, we find $\sigma_\star \sim 83$ km/s (i.e. $\log(\sigma_\star/(\mathrm{km/s})) \sim 1.92$). We adopt an uncertainty of 0.10 dex to account for the scatter found in the relation by Bezanson et al. (2018).

From our spaxel-by-spaxel fitting of the high-resolution data (see Sect. 3.1), we find a fairly smooth velocity gradient of about $\Delta v \sim 100$ km/s based on the narrow line emission across the main galaxy component (see Appendix E). This may be used together with the velocity dispersion to constrain the galaxy kinematics and to construct a dynamical mass model. However, the possibility of an ongoing galaxy merger based on the NIRCam imaging and/or the evidence of a second massive black hole in the centre of J0148-4214 complicates the modelling. We defer a more detailed analysis of the galaxy kinematics of this source to future work. For the purpose of the present analysis, we attempt a simple first-order estimate of the total mass of J0148-4214 by approximating $M_{\mathrm{dyn}} \sim 5\sigma_\star^2 R_e/G$ (Cappellari et al. 2006). Here, G is the gravitational constant, and R_e is the effective radius which we estimate from the major axis of a two-dimensional Gaussian fit to the [O III] line map, correcting for the approximate PSF at this wavelength ($\mathrm{PSF}_{\mathrm{FWHM,[OIII]}} \sim 0.185''$) through subtraction in quadrature. With this approach, we find $R_e \sim 0.64$ kpc and $\log(M_{\mathrm{dyn}}/M_\odot) \sim 9.7$. This estimate could be further refined through constraints on the structural parameters, specifically the Sérsic index n and projected axis ratio q. Adopting common combinations of these param-

Table 2. Black hole properties.

	$\mathrm{FWHM}_{\mathrm{H}\alpha,\mathrm{BLR}}$ [km/s]	$L_{\mathrm{H}\alpha,\mathrm{BLR}}$ [10^{42} erg/s]	$\log(M_\bullet/M_\odot)_{\mathrm{H}\alpha}$	$\log(L_{\mathrm{bol}}/(\mathrm{erg/s}))_{\mathrm{H}\alpha,\mathrm{BLR}}$	$\log(\lambda_{\mathrm{Edd}})$	$d_{\mathrm{I},i}$ [kpc]	Δv [km/s]
AGN I	2920 ± 140	$4.80^{+0.37}_{-0.38}$	7.9 ± 0.4	44.8 ± 0.6	-1.18 ± 0.74		110
AGN II	430 ± 80	$1.03^{+0.22}_{-0.23}$	5.8 ± 0.5	44.1 ± 0.6	0.18 ± 0.77	0.19 ± 0.04	228
AGN III	1060 ± 170	0.16 ± 0.04	6.3 ± 0.5	43.3 ± 0.6	-1.07 ± 0.62	$\sim$1.66	3

Notes. Properties of the massive black holes in J0148-4214 and related measurements from the high-resolution data. Measurements for the primary AGN I and AGN II are extracted from our best fit to the main galaxy aperture spectrum; properties for AGN III are extracted from the best fit to the NW black hole aperture spectrum. The projected distances $d_{\mathrm{I},i}$ are with respect to the primary AGN I. $d_{\mathrm{I,II}}$ is obtained from the channel map centroids (Sect. 3.1), while $d_{\mathrm{I,III}}$ is an approximation. Relative velocities of the BLR components Δv are reported with respect to the narrow Hα emission from the main galaxy aperture spectrum.

eters ($n \in [0.5; 8]$; $q \in [0.2; 1]$) and using the calibrations by van der Wel et al. (2022), our dynamical mass estimates for J0148-4214 vary in the range $\log(M_{\mathrm{dyn}}/M_\odot) \sim 9.5$–$10.2$. In any case, our stellar mass estimate of $\log(M_\star/M_\odot) = 9.1$ is lower than M_{dyn}, allowing for 2.5 times or more additional mass in the form of gas and dark matter.

5. The black holes in J0148-4214

5.1. Masses

We used the single-epoch calibration by Reines et al. (2013) to estimate the masses of the black holes in J0148-4214 based on the best-fit FWHMs and luminosities of the Hα BLR components[3] (without dust correction). The corresponding measurements and results are reported in Table 2. Listed uncertainties on black hole masses are dominated by the scatter in local scaling relations. We adopt a value of 0.4 dex (e.g. Ho & Kim 2014) which we add in quadrature to the propagated uncertainties from our best-fit results. We find black hole masses of $\log(M_\bullet/M_\odot) = 7.9 \pm 0.4, 5.8 \pm 0.5$ and 6.3 ± 0.5 for the primary central AGN (I), the lower-mass central AGN (II), and the north-western AGN (III), respectively (or BH_1, BH_2, BH_3, respectively). If our interpretation is correct, BH_2 is among the lowest-mass black holes so far discovered above $z \sim 5$ (see Sect. 5.4). There is one AGN candidate by Maiolino et al. (2024a) with a lower mass estimate of $\log(M_\bullet/M_\odot) = 5.65 \pm 0.31$ (they assume an intrinsic scatter of 0.3 dex for the local scaling relation), which was interestingly also identified as a possible secondary AGN in a system at $z \sim 5.9$ through NIRSpec-MSA slit spectroscopy within the JADES programme. Our program BlackTHUNDER is carrying out NIRSpec-IFS observations of this target at both low and high spectral resolution, which will be crucial to confirm the nature of this system.

While the stellar mass estimate for J0148-4214 is within the mass range of the local low-luminosity AGNs used to derive the scaling relation by Reines et al. (2013), it is not entirely clear whether such local scaling relations can be applied to higher-z broad-line AGNs. There are indications that these estimates may carry systematic uncertainties of 0.5−1 dex, as we detail in the following. Recently, Greene et al. (2026) argued that the bolometric luminosities of a sub-class of high-z AGNs, the so-called little red dots (Matthee et al. 2024), could be overestimated by an order of magnitude. Then, there are some indications that the geometry of many of the high-z BLRs could be different: ubiquitous absorption features in the broad lines of hydrogen and helium as well as the lack of X-ray detections for the majority of these AGNs suggest that the covering factor of high-z BLRs could be significantly higher than typical in local AGNs (e.g. Matthee et al. 2024; Juodžbalis et al. 2024a; Ji et al. 2025; Loiacono et al. 2025; D'Eugenio et al. 2026b,a; Maiolino et al. 2025). This could introduce a systematic overestimation of the high-z black holes masses by factors of two to three (0.3−0.5 dex in log). Similarly, it has been pointed out that if the black holes are accreting at super-Eddington levels, their BLR sizes would be smaller, for a given black hole mass, leading to an overestimation of their masses when using standard single-epoch relations calibrated on sub-Eddington samples. This could reduce black hole masses by up to 0.5–1 dex and may at the same time explain their X-ray weakness (Lupi et al. 2024; Lambrides et al. 2026; Inayoshi et al. 2025). On the other hand, at (super-)Eddington accretion, radiation pressure can result in a lower effective gravitational force felt by the BLR clouds, and thus, a lower observed FWHM of the BLR lines, which in turn would lead to an underestimation of black holes masses (see Marconi et al. 2008).

To date, the most accurate black hole mass measurements at high redshifts are obtained by resolving the BLRs of luminous quasars through interferometry with VLTI/GRAVITY+. So far, the masses of four (and upper limit for one) $z \sim 2$ black holes have been obtained with this method (Abuter et al. 2024; GRAVITY+ Collaboration, in prep.). These measurements indicate that the masses inferred from the single-epoch calibration by Reines et al. (2013) applied to the Hα BLR emission could overestimate high-z black hole masses by factors of two to ten. Interestingly, the authors also find that the quasars observed in their studies are accreting at highly super-Eddington rates, with a BLR size significantly smaller than expected from local relations. A recent study by Parlanti et al. (2025b) of five $z \sim 2$ AGNs suggests that the masses of black holes with lower accretion rates could still be estimated with local scaling relations. GRAVITY+ Collaboration (2026) made the first measurement of a quasar accreting at super-Eddington rates at $z \sim 4$, finding a black hole mass one order of magnitude smaller compared to estimates from single-epoch scaling relations. This source has a strong outflow (resulting in a prominent, blue-shifted wing of Hβ), and if the scaling relations are applied only to the discy part of the BLR, they are in better agreement with the BLR dynamical measurement.

A dynamical mass estimate (or lower limit) for the black hole in a low-luminosity AGN at $z = 7.04$ has recently been obtained within the BlackTHUNDER programme, through a spatially resolved spectroscopic measurement of the lensed source Abell2744-QSO1 (Juodžbalis et al. 2026b). In this case, the dynamical measurement is consistent with black hole mass estimates from single-epoch methods using the Hα or Hβ BLR

[3] Masses estimated from the single-epoch calibrations by Greene & Ho (2005) are about 0.2–0.4 dex (0.6 dex) lower using the Hα (Hβ) BLR components for the AGN in J0148-4214.

components (Furtak et al. 2024; Ji et al. 2025; D'Eugenio et al. 2026b; Maiolino et al. 2026).

Recently, it has also been proposed that the broad-line shapes seen in compact, high-z AGNs do not trace solely the BLR, but are broadened by various scattering mechanisms (Rusakov et al. 2026; Naidu et al. 2025; Chang et al. 2026), such that the intrinsic, narrower BLR lines would correspond to much lower black hole masses, by up to two orders of magnitude. While this may be the case for some objects, Juodžbalis et al. (2026a) and Brazzini et al. (2025) have shown that these proposed mechanisms do not generally apply to low-luminosity AGNs at high redshifts (see also Juodžbalis et al. 2026b).

The focus of this work is not the accurate determination of the black hole masses, but the discovery of three massive, active black holes in a galaxy just 1.2 Gyr after the Big Bang. Therefore, for the purpose of this paper, we proceed with the black hole masses derived following the local single-epoch method, but emphasise that these estimates come with substantial uncertainties.

5.2. Luminosities and Eddington ratios

We calculate the bolometric luminosities following Eq. (6) by Stern & Laor (2012) which utilises the Hα BLR luminosity, and find $\log(L_{\rm bol}/({\rm erg/s})) = 44.8 \pm 0.6$, 44.1 ± 0.6 and 43.3 ± 0.6 for AGNs I, II, and III. Our estimate for AGN I is consistent with the value of $\log(L_{\rm bol}/({\rm erg/s})) = 44.8$ derived by Matthee et al. (2024) using another calibration based on the Hα BLR flux (Greene & Ho 2005; Richards et al. 2006). We note that different calibrations utilizing the narrow line widths of Hβ, for example, under the assumption that the narrow line emission is dominated by the AGN (e.g. Netzer 2019), can yield bolometric luminosities of about one order of magnitude higher for AGN I (see also Perna et al. 2023; Übler et al. 2023).

We infer the Eddington luminosity $L_{\rm Edd}$ of the black holes in J0148-4214 using our estimates of $M_\bullet$. We calculate Eddington ratios of $\log(\lambda_{\rm Edd}) = \log(L_{\rm bol}/L_{\rm Edd}) = -1.18 \pm 0.74$, 0.18 ± 0.77 and -1.07 ± 0.62 for AGNs I, II, and III, respectively. It is interesting to see that the lower-mass black hole in the centre shows super-Eddington accretion, while the larger primary black hole accretes at sub-Eddington levels. This is quantitatively similar to the results by Maiolino et al. (2024a) who also find that the secondary AGNs in their dual AGN candidate galaxies accrete at Eddington or super-Eddington rates, while the respective primary AGNs accrete at sub-Eddington rates. From the theoretical point of view, some models studying the accretion rates onto massive black holes in binary systems find preferential accretion rates on the secondary (lower-mass) black holes (e.g. Farris et al. 2014; Duffell et al. 2020; Siwek et al. 2023); however others do not (e.g. Ochi et al. 2005; Hanawa et al. 2010; Bourne et al. 2024). In the observational study by Maiolino et al. (2024a), all high-z AGNs with $\log(M_\bullet/M_\odot) \lesssim 6$ accrete at or above the Eddington limit. As discussed by the authors, this may be due to selection effects, because it would be harder to detect smaller black holes accreting at low Eddington rates (see also discussion by Juodžbalis et al. 2024b). It is therefore worthwhile noting the sub-Eddington accretion rate of the off-nuclear $\log(M_\bullet/M_\odot) = 6.2$ black hole in the north-west of J0148-4214, opening up a regime of low black hole mass and low accretion rate, so far unpopulated by moderate-luminosity high-z AGNs.

5.3. Narrow-line ratio diagnostics

The classical narrow line ratio diagnostics involving the strong rest-frame optical lines Hβ, [O III], Hα, [N II] and $[{\rm S\,II}]_{6717,6731}$ routinely used to identify AGNs (Baldwin et al. 1981; Veilleux & Osterbrock 1987) have been shown to no longer be effective for many high-z AGNs, likely due to their low metallicities (see Kewley et al. 2013a,b; Nakajima & Maiolino 2022; Kocevski et al. 2023; Übler et al. 2023; Harikane et al. 2023; Maiolino et al. 2024a; Arevalo-Gonzalez et al. 2025; Scholtz et al. 2025). Instead, AGNs start to overlap with star-forming galaxies, which also shift locus in these diagrams due to different ISM conditions and abundance compositions of ionizing massive stars (e.g. Shapley et al. 2025). J0148-4214 falls into the regime of $z = 0$ star-forming galaxies on the [O III]/Hβ vs. [N II]/Hα and [O III]/Hβ vs. $[{\rm S\,II}]_{6717,6731}$/H$\alpha$ diagnostic diagrams, and would therefore be misclassified as a star-forming galaxy if using these classical diagnostics. Only in the [O III]/Hβ vs. $[{\rm O\,I}]_{6300}$/Hα diagram would J0148-4214 be classified as an AGN (see also Juodžbalis et al. 2026a).

Mazzolari et al. (2024) proposed utilising the $[{\rm O\,III}]_{4363}$/Hγ narrow line ratio together with other rest-frame optical line ratios to robustly identify AGNs even at low metallicities (see also Übler et al. 2024b). Unfortunately in the case of J0148-4214, $[{\rm O\,III}]_{4363}$ is not covered with the high-resolution grating, and blended with Hγ in the prism observations. However, we can explore several rest-frame UV diagnostic diagrams (see Table D.1), but caution that in the case of J0148-4214 the uncertainties are large for all rest-frame UV diagnostics explored. In the $[{\rm C\,III}]_{1909}$/$[{\rm He\,II}]_{1640}$ vs. $[{\rm C\,IV}]_{1546,1551}$/$[{\rm C\,III}]_{1909}$ diagram, J0148-4214 falls just at the separation of AGNs and composite galaxies based on the demarcation by Hirschmann et al. (2019). In both the C IV/C III] vs. (C III]+C IV)/$[{\rm He\,II}]_{1640}$ and the EW($[{\rm He\,II}]_{1640}$/Å) vs. C III]/$[{\rm He\,II}]_{1640}$ or vs. C IV/$[{\rm He\,II}]_{1640}$ diagrams, J0148-4214 falls into the regime populated by AGN models according to Nakajima & Maiolino (2022). These results underline the suitability of rest-frame UV line ratio diagnostics to identify AGNs also for high-z, low-metallicity black holes, although higher spectral resolution and higher S/N observations would be helpful to explore the rest-frame UV emission of J0148-4214 in more detail.

5.4. Scaling relations with host galaxy properties

In Fig. 3 we plot the masses of the black holes in J0148-4214 as a function of stellar mass. Here, we initially use the total stellar mass derived from SED fitting as described in Sect. 4.1 as a reference for all three black holes (filled blue stars). We compare our measurements to a sample of low-luminosity AGNs in the local Universe by Reines & Volonteri (2015) together with their scaling relation (grey points and black line), the local scaling relation by Greene et al. (2020, dash-dotted line), and to a number of high-z AGNs discovered or studied with JWST (Übler et al. 2023; Perna et al. 2023; Parlanti et al. 2024; Tripodi et al. 2025b; Marshall et al. 2025; Akins et al. 2025; Juodžbalis et al. 2026a; D'Eugenio et al. 2026a; Maiolino et al. 2024b, 2026; Rinaldi et al. 2025; Taylor et al. 2025; Zhang et al. 2026; Jones et al. 2026b).

As noted by many authors, the majority of JWST-discovered AGNs lie above the local scaling relations, although some sources fall within the scatter of local measurements (e.g. Harikane et al. 2023; Kokorev et al. 2023; Furtak et al. 2024; Maiolino et al. 2024a; Juodžbalis et al. 2026a; Li et al. 2026). The primary AGN of J0148-4214 (large filled blue star) has a similar offset from the local relation as other low-luminosity AGNs at similar redshifts. In contrast, the two lower-mass black holes in the centre and the NW black hole (smaller filled blue stars) fall within the scatter of local measurements when we

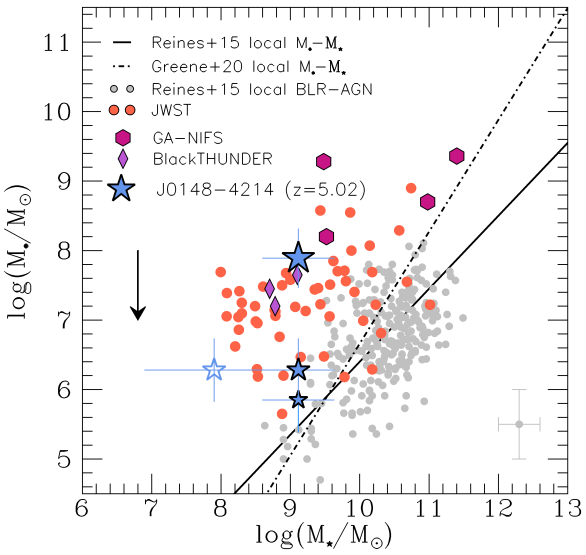

Fig. 3. Black hole mass as a function of host galaxy stellar mass. We show the black holes in J0148-4214 as filled blue stars, other BlackTHUNDER sources as purple diamonds (D'Eugenio et al. 2026a; Maiolino et al. 2026; Jones et al. 2026b), sources from the GA-NIFS survey as pink hexagons (Übler et al. 2023; Perna et al. 2023; Parlanti et al. 2024; Marshall et al. 2025), sources from the JADES survey (Maiolino et al. 2024a; Juodžbalis et al. 2026a) and a number of other studies (Tripodi et al. 2025b; Akins et al. 2025; Maiolino et al. 2024b; Rinaldi et al. 2025; Taylor et al. 2025; Zhang et al. 2026) as orange circles, and data from local AGNs in grey (Reines & Volonteri 2015). Local relations by Reines & Volonteri (2015) and Greene et al. (2020) are shown as solid and dash-dotted lines, respectively. The black arrow indicates a potential downward correction of one order of magnitude, based on considerations regarding the high-z BLR geometry (see Sect. 5.1 for details). The primary black hole in J0148-4214 appears overmassive compared to the local relations, while the two lower-mass black holes in J0148-4214 fall within the scatter of the local relations. The open blue star indicates the position of the NW black hole if a separate estimate of the stellar mass of the north-western region of J0148-4214 is considered (see Sect. 5.4 for details).

use the total stellar mass of J0148-4214 as a reference. However, the stellar mass associated with the NW black hole would be different if this is in the process of being accreted onto the main galaxy, for example through a minor merger. We attempt to constrain the stellar mass of the NW region specifically, by (i) repeating our SED fitting for an aperture extraction of three-by-three pixels centred on the NW black hole, and by (ii) assuming that the continuum tail seen in the NIRCam imaging is dominated by stellar continuum with the same mass-to-light ratio as the main galaxy, and scaling our total mass estimate based on the surface brightness ratio determined from the F115W imaging. While both of these approaches are strongly limited by the low S/N in this region as well as PSF effects which are unaccounted for, we find approximate masses of $\log(M_\star/M_\odot)_{\rm NW} = 8.0 \pm 0.6$ and 7.8 ± 0.8. The averages of these estimates and the corresponding position of the NW black hole are indicated in Fig. 3 as an open blue star. If the so approximated stellar mass does correspond to a companion galaxy, also the NW black hole should be considered overmassive with respect to local AGNs, although we caution that in this case some of the original stellar mass associated with the companion could have been tidally stripped (e.g. Yu 2002; Volonteri et al. 2022). On the other hand, if the NW black hole is instead in the process of being ejected from J0148-4214 following a three-body interaction with the two central black holes, or as a consequence of a previous massive black hole merger (i.e. a recoil black hole), assigning the main host stellar mass also to BH_3 is still reasonable (see also discussion in Sect. 5.5 and the tentative kinematic evidence discussed in Appendix E). The secondary black hole in the centre may have formed in situ in J0148-4214, in which case assigning the host stellar mass is reasonable. However, it could also have been accreted through a previous galaxy merger. Due to the small separation of the two central black holes there is no hope of identifying or determining a potential separate stellar mass component for BH_2 from current data. Considering also the smooth central ISM kinematics (see Appendix E), we consider the secondary BH fully embedded in J0148-4214 at the time of observation. In the future, larger datasets of high-z black hole multiplets could provide a way to statistically investigate their origins (see e.g. Lupi et al. 2021; Zhang et al. 2024).

It has been pointed out that the prevalence of overmassive, moderate-luminosity black holes at high redshifts in the $M_\bullet - M_\star$ plane may be due to selection bias and sensitivity limits, coupled with a higher dispersion of the relation (Li et al. 2025; see also Silverman et al. 2025 for luminous quasars). Stacking exercises for sources without individual AGN detections (either Type I or Type II) at $3 < z < 7$ have revealed average black hole masses much closer to local relations (Geris et al. 2026). A recent study by Ren et al. (2025) finds one robust and six candidate Type I AGNs in $z \sim 4.4$–5.7 main-sequence galaxies from the ALPINE-CRISTAL-JWST survey (Faisst et al. 2026) which are consistent with local relations. Certainly, there exists a large and likely dominant population of lower-mass black holes at high redshifts, which has not been detected in current JWST datasets due to selection biases and sensitivity limitations. Such a population has been modelled by cosmological simulations of galaxy formation (e.g. Sijacki et al. 2007, 2015; Volonteri et al. 2020; Jeon et al. 2023; Habouzit et al. 2022; Habouzit 2025). However, even if the offset of the $M_\bullet - M_\star$ relation at high z is dominated by selection effects, the finding of overmassive black holes (even when accounting for possible systematics; see Sect. 5.1) which constitute a significant fraction of their entire host galaxy mass, like the primary AGN in J0148-4214, is remarkable. This population provides informative constraints on possible black hole seeding and growth mechanisms in the early Universe (e.g. Schneider et al. 2023; Natarajan et al. 2024; Regan & Volonteri 2024). Finally, we note that overmassive black holes have been detected to exist also at later cosmic times (e.g. around $z \sim 0.5$–3; Mezcua et al. 2023, 2024).

The black holes in this study exist just 1.15 Gyr after the Big Bang. We can expect that they and their host galaxy will grow by a substantial amount during the more than 12 Gyr time span until the present day. The comparison with local, moderate-luminosity AGNs therefore serves merely to highlight any differences of these early AGNs with local, similarly active galaxies. It is likely that our high-z AGNs will grow into massive, evolved galaxies by $z = 0$. In the local Universe, the black hole masses of such systems are typically compared to the stellar mass or velocity dispersion of the bulge component (with bulge-to-total fractions reaching up to $B/T = 1$) of their host galaxies (e.g. Ferrarese & Merritt 2000; Kormendy & Ho 2013; McConnell & Ma 2013; Bennert et al. 2015). In Fig. 4 we plot the masses of black holes in J0148-4214 as a function of stellar velocity dispersion (see Sect. 4.2). Again, we initially use the value for the main galaxy as reference for all black holes in J0148-4214, but we also show a separate estimate for the NW black hole (open blue star), based on $\sigma_\star$ inferred from the [O III]$_{5007}$ line from the NW extraction (see Sect. 4.2 for the assumptions

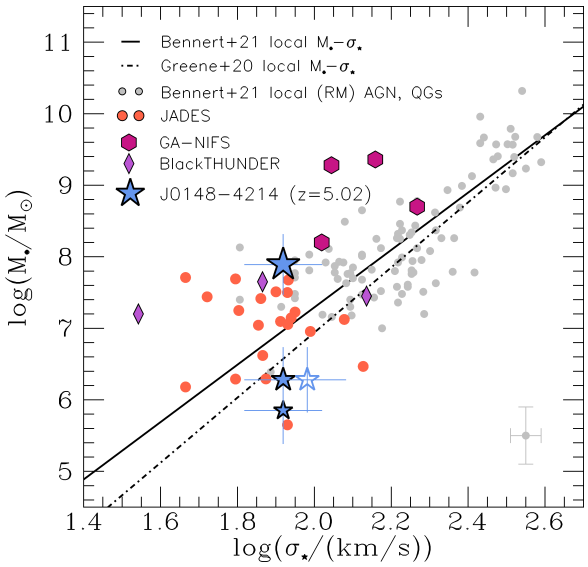

Fig. 4. Black hole mass as a function of stellar velocity dispersion. We show the black holes in J0148-4214 as filled blue stars, other BlackTHUNDER sources as purple diamonds (D'Eugenio et al. 2026a; Maiolino et al. 2026; Jones et al. 2026b), sources from the GA-NIFS survey as pink hexagons (Übler et al. 2023; Perna et al. 2023; Parlanti et al. 2024; Marshall et al. 2025), sources from the JADES survey as orange circles (Maiolino et al. 2024a; Juodžbalis et al. 2026a), and data from local AGNs and quiescent galaxies (QGs) in grey (Kormendy & Ho 2013; Bennert et al. 2021). Local relations by Bennert et al. (2021) and Greene et al. (2020) are shown as solid and dash-dotted lines, respectively. For high-z literature sources, we (re-)calculated $\sigma_\star$ according to Bezanson et al. (2018) as described in Sect. 4.2. The black holes in J0148-4214 scatter around the local relations, even when a separate $\sigma_\star$ estimate is considered for the NW black hole (open blue star; see Sect. 5.4 for details).

involved)[4]. Maiolino et al. (2024a) pointed out that the majority of high-z AGNs that appear overmassive in the $M_\bullet - M_\star$ plane are more consistent with local galaxies in the $M_\bullet - \sigma_\star$ plane (see also Juodžbalis et al. 2026a). Also the black holes in J0148-4214 are spread around the low-$\sigma_\star$ end of the local relations by Bennert et al. (2021) and Greene et al. (2020). This could indicate that high-z galaxies such as J0148-4214 evolve along the $M_\bullet - \sigma_\star$ relation until the present day (see also Jahnke & Macciò 2011). Since the integrated velocity dispersion is a proxy for the total dynamical mass of a system, it may also indicate that the total mass typically associated with local (quiescent) black holes is already in place at early times, in the form of gas and/or dark matter (e.g. McClymont et al. 2026). This would imply that, on average, galaxies (not just their stellar content) and massive black holes do grow together over most of cosmic history. Ideally, independent measurements of the galaxy gas mass would help to further investigate the relation between the total baryon content and black hole mass at these early cosmic epochs.

We also note that the increase in scatter seen at the lower end of the $M_\bullet - \sigma_\star$ relation could be a result of the highly dynamic evolution of massive black hole binaries or multiplets at early cosmic times, which may drive galaxies temporarily off the main relation. For instance, the ejection of a massive black hole would move a galaxy below the relation (e.g. Mannerkoski et al. 2022), while the potential capture of a massive, solitary black hole could move a galaxy above the relation. The latter, however, is certainly a less likely event, and other physical processes or larger intrinsic uncertainties should be considered as possible reasons for the increased scatter above the relation at the low-$\sigma_\star$ end. For instance, a smaller scatter at the high-mass end could simply be the result of a higher number of black hole mergers (Hirschmann et al. 2010). We note, however, that recently a population of ultra-massive black holes has been identified in the local Universe, which are positive outliers on the high-mass end of the $M_\bullet - \sigma_\star$ relation (Saglia et al. 2024; de Nicola et al. 2025). Clearly, the topic of the scatter in the $M_\bullet - \sigma_\star$ relation requires further investigation. Ultimately, statistical investigations of the scatter at the low-$M_\bullet$ end may provide insights into the formation channels of black holes.

5.5. What is the fate of the massive black holes in J0148-4214?

Close-separation dual or triple black holes such as those discovered in this work are of great interest in the context of black hole growth, since they are likely going to merge by $z = 0$. From the theoretical perspective, massive black hole triplets and their subsequent mergers have been studied in a number of models and across a range of scales (e.g. Volonteri et al. 2003; Hoffman & Loeb 2007; Kulkarni & Loeb 2012; Bonetti et al. 2018; Ryu et al. 2018; Mannerkoski et al. 2021; Partmann et al. 2024; Buttigieg et al. 2025; Rantala et al. 2025).

We first consider the massive primary black hole together with the lower-mass black hole in the central region of J0148-4214. From mapping the emission of the two BLRs of these black holes, we derived a projected separation of 190 ± 40 pc (Sect. 3.1). We note that the sphere of influence of the primary black hole is about $r_h \sim 50$ pc (with $r_h = GM_\bullet/\sigma^2_{\star,\mathrm{bulge}}$, assuming $\sigma_{\star,\mathrm{bulge}} = \sigma_\star$; see Sect. 4.2); this means that for a circular orbit the two central black holes are not (yet) gravitationally bound, although this may be different in the case of an eccentric orbit. Even if unbound, at these separations and considering the total stellar mass and size of the system, the two black holes are likely already in the efficient dynamical friction phase (Chandrasekhar 1943; Ostriker & Tremaine 1975; Begelman et al. 1980; Ostriker 1999). This process, during which the interaction of the black holes with the stars, gas and dark matter around them promotes the loss of angular momentum, precedes the later stages of massive black hole mergers – the stellar hardening phase, reached at a separation of about $a_h = GM_{\bullet,2}/(4\sigma^2_\star) \sim 0.1$ pc for the two central black holes in J0148-4214 (Begelman et al. 1980; Quinlan 1996; $M_{\bullet,2}$ being the mass of the lighter black hole), and eventually the emission of gravitational waves leading to the coalescence of the black holes (Peters & Mathews 1963; Peters 1964).

We use our black hole mass estimates together with the total stellar mass of J0148-4214 extracted from a 1.7 kpc radius aperture ($\log(M_\star/M_\odot) = 9.1$; Sect. 4.1), and assume an absolute separation of the two central black holes of 0.3 kpc. Following Binney & Tremaine (2008), we calculate the dynamical friction time for the secondary black hole BH_2 with mass M to reach the primary one as $t_{\mathrm{df}} = 1.65/\ln(\Lambda) \cdot (r_i^2\sigma_\star)/(GM)$, with $r_i = 0.3$ kpc, and $\Lambda \approx b_{\max} v^2_{\mathrm{typ}}/(GM)$. Here, $v^2_{\mathrm{typ}} \approx GM_\star/R_e$, and we assume $b_{\max} = 0.3$ kpc. We find an approximate inspiral time of $t_{\mathrm{df}} \sim 0.66$ Gyr (corresponding to $z \sim 3.5$). We emphasise that this simplistic calculation neglects contributions from gas and dark matter which may shorten the dynamical friction time. If we use M_{dyn} instead of $M_\star$ in the above calculation, we find $t_{\mathrm{df}} \sim 0.55$ Gyr ($z \sim 3.65$); however, we stress that neither

[4] Using instead the Hα narrow line measured from the NW extraction ($\sigma_{\mathrm{H}\alpha,\mathrm{n}} = 14^{+16}_{-14}$ km/s) would result in a poorly constrained value of $\log(\sigma_\star/(\mathrm{km/s})) \sim 1.35 \pm 0.51$, arguably too low compared to the spectral resolution of NIRSpec to be trustworthy.

approach properly accounts for the effects of the dissipative gas component. The off-nuclear black hole may also be in the process of sinking towards the galaxy centre (we discuss alternative scenarios further below). Using the same approach as above, and considering $r_i \sim b_{\rm max} \sim 1.7$ kpc and our estimate for $M_\star$, we find an approximate inspiral time of $t_{\rm df} \sim 5.9$ Gyr (corresponding to $z \sim 0.75$). If we use $M_{\rm dyn}$ instead, we find $t_{\rm df} \sim 5.0$ Gyr ($z \sim 0.93$). We note that the detection of not just two but three massive black holes in such close proximity is relevant in this context, since triple black hole interactions provide a mechanism to promote and accelerate the merging of massive black holes (e.g. Saslaw et al. 1974; Hills & Fullerton 1980; Blaes et al. 2002; Colpi et al. 2002; Ryu et al. 2018; Bonetti et al. 2019; Mannerkoski et al. 2022; Sayeb et al. 2024).

Assuming that the black holes will merge by the present day after the dynamical friction phase, the eventual massive black hole mergers in descendants of systems such as J0148-4214 may be detectable by the next-generation gravitational wave detector Laser Interferometer Space Antenna (LISA; Thorne & Braginskii 1976; Amaro-Seoane et al. 2023). At the time of observation, the mass ratios $q = m_i/m_j$ for the black holes in J0148-4214 are $q = 0.008$ for $\rm BH_1$ and $\rm BH_2$ and $q = 0.025$ for $\rm BH_1$ and $\rm BH_3$ (or $\rm BH_{1+2}$ and $\rm BH_3$). The corresponding chirp masses $\mathcal{M} = (m_i \cdot m_j)^{3/5}/(m_i + m_j)^{1/5}$ (assuming no significant mass growth prior to coalescence) are $\mathcal{M} = 10^{6.6}$ for $\rm BH_1$ and $\rm BH_2$ and $\mathcal{M} = 10^{6.9}$ for $\rm BH_1$ and $\rm BH_3$ (or $\rm BH_{1+2}$ and $\rm BH_3$). To obtain some first-order constraints on the potential detection probability with LISA, we use the simulator `GWFish` (Dupletsa et al. 2023). We emphasise that we make the simplifying assumptions of no further mass growth of the black holes, and that the black holes actually merge after the dynamical friction times calculated above. We further neglect spinning and precession of the black holes and apply the `IMRPhenomXHM` waveform model (García-Quirós et al. 2020). As an additional caveat, we note that we treat the mergers of $\rm BH_1$ with $\rm BH_2$ and of $\rm BH_{1+2}$ with $\rm BH_3$ separately. In reality, as mentioned above, depending on the black hole separations and the masses of the black holes and host galaxy involved, it is also possible that the third black hole influences the gravitational wave signal of the binary (e.g. Bonetti et al. 2019; Ficarra et al. 2023). Sampling 100 realisations of our measured black hole masses within the quoted uncertainties, and random angular parameters, we obtain a detection probability of 38.2 ± 4.2 per cent for the merger of $\rm BH_1$ and $\rm BH_2$, and 81.8 ± 1.8 for $\rm BH_{1+2}$ and $\rm BH_3$, with a mean S/N of 24.6 ± 2.4 and 279.5 ± 11.8, respectively. If we consider the shorter dynamical friction times obtained from using $M_{\rm dyn}$ instead of $M_\star$, we find somewhat reduced detection probabilities of 24.2 ± 1.9 and 78.2 ± 0.8 per cent. While a number of simplifications and uncertainties are attached to these calculations, this highlights that the descendants of systems such as J0148-4214 may be plausible candidates for LISA detections. In principle, the potential late-time mergers of massive black holes such as in J0148-4214 could also contribute to the gravitational wave background detected by the Pulsar Timing Array (PTA) collaborations (Agazie et al. 2023, 2024; EPTA Collaboration et al. 2024).

As mentioned earlier, an alternative fate for $\rm BH_3$ may be the expulsion from the J0148-4214 system, considering that it could have been ejected from the centre through a three-body interaction with the other two massive black holes, or through a recoil kick as the consequence of a previous massive black hole merger (e.g. Peres 1962; Bekenstein 1973; Saslaw et al. 1974; Mikkola & Valtonen 1990; Volonteri et al. 2003; Madau & Quataert 2004; Merritt et al. 2004; Blecha et al. 2016; Sijacki et al. 2011; Mannerkoski et al. 2022; Dong-Páez et al. 2025). In this scenario, if $\rm BH_3$ were able to leave the parent halo of J0148-4214, dragging some small amount of gas, stars, and dark matter with it, it could appear as a heavily overmassive, nearly solitary black hole at later times. This could resemble observations of high-z massive black holes with little evidence of (much of) a host galaxy around them (see Chen et al. 2025; Maiolino et al. 2026; Juodžbalis et al. 2026b). According to theoretical models, such solitary black holes resulting from three-body interactions may not be uncommon (Volonteri et al. 2003). However, it is unclear whether the ejected black hole would be able to retain any additional material (e.g. Partmann et al. 2024) and, therefore, specifically considering gas, whether it would be visible in accretion or not. If instead ejected through a gravitational wave recoil from a previous massive black hole merger, the retention of a compact, bound star cluster would be expected (e.g. O'Leary & Loeb 2009; Merritt et al. 2004; Rawlings et al. 2025). Since $\rm BH_3$ is accreting material at the time of observation, a recoil event could therefore be more likely than a three-body interaction. The fact that $\rm BH_3$ is not the lightest of the three black holes would further favour a recoil event over a three-body interaction (Saslaw et al. 1974). In this scenario, the $\gtrsim$1.7 kpc separation from the galaxy centre suggests at least a moderate kick velocity of $\gtrsim$200 km/s in order to exceed the galaxy escape velocity. This in turn implies a mass ratio of the progenitor black hole binary $q \gtrsim 0.1$ (e.g. Tanaka & Haiman 2009). With a remnant mass of $\log(M_\bullet/M_\odot) \sim 6.3$, this would therefore be an ideal LISA target, detectable at high redshifts with high S/N (see e.g. Valiante et al. 2021; Liu & Inayoshi 2025).

It is also a possibility that the NW black hole has been ejected previously, but will be re-accreted into the centre to eventually merge with the other two central black holes. From the theoretical perspective, such an evolutionary pathway has been described in detail in a cosmological context by Mannerkoski et al. (2021), predicting situations which are comparable to our observations in terms of the distances of the three black holes, although for black holes with higher and more similar masses ($\log(M_\bullet/M_\odot) \sim 8.0-8.9$), and for later cosmic times ($z < 1$).

6. Conclusions

In this work we have presented new NIRSpec-IFU data of the $z \sim 5$ galaxy J0148-4214, revealing multiple Hα broad-line regions. Through detailed analysis of the spatially resolved data, and after discarding alternative interpretations such as supernovae, shocks, winds, or massive stars, we conclude that the observations are compatible with three massive ($M_\bullet \sim 10^{5.8-7.9}\,M_\odot$) accreting black holes. This discovery of a black hole triplet at high redshifts might indicate that multiple massive black hole systems are common in the early Universe. In J0148-4214, two of the black holes are already in close proximity, at a projected separation of about 190 ± 40 pc. While the integrated spectrum from the NIRCam grism observations showed an indication of a complex BLR profile, only the spectral mapping capabilities of the NIRSpec-IFU allowed us to disentangle the BLR profile and to separate the two black holes spatially. Similarly, the discovery of the third faint black hole at a projected distance of about 1.7 kpc from the central black hole binary would not have been possible without the IFU. Additional data at higher spatial and spectral resolution will help to investigate in greater detail the dynamics of this system, and to achieve a refined characterisation of the central region of J0148-4214. Several integrated spectra of high-z AGNs show BLR shapes comparable to J0148-4214, indicating that they too could host dual or multiple AGNs. These systems require NIRSpec-IFU observa-

tions to be confirmed. Our results highlight the crucial role of IFU observations in discovering massive black hole multiplets in galaxies in the early Universe, the progenitors of massive black hole mergers. Such black hole mergers, with the masses and timescales estimated in this work, may be detectable by next-generation gravitational wave observatories such as LISA.

Acknowledgements. We thank the anonymous referee for a constructive report that helped to improve the quality of this manuscript. We thank Stephanie Buttigieg, Filippo Mannucci, Thorsten Naab and Michael Kramer for valuable comments. We are grateful to Vardha Bennert for sharing a machine-readable version of Table 3 by Bennert et al. (2021). HÜ thanks the Max Planck Society for support through the Lise Meitner Excellence Program. HÜ and GM acknowledge funding by the European Union (ERC APEX, 101164796). NMFS and GT acknowledge funding by by the European Union (ERC, GALPHYS, 101055023). RM, FDE, LRI, and GCJ acknowledge support by the Science and Technology Facilities Council (STFC), by the ERC through Advanced Grant 695671 "QUENCH", and by the UKRI Frontier Research grant RISEandFALL. RM also acknowledges funding from a research professorship from the Royal Society. SA acknowledges grant PID2021-127718NB-I00 funded by the Spanish Ministry of Science and Innovation/State Agency of Research (MICIN/AEI/ 10.13039/501100011033). GC and EB acknowledge financial support from INAF under the Large Grant 2022 "The metal circle: a new sharp view of the baryon cycle up to Cosmic Dawn with the latest generation IFU facilities" and from the INAF GO grant 2024 "A JWST/MIRI MIRACLE: MidIR Activity of Circumnuclear Line Emission". EB also acknowledges support from the "Ricerca Fondamentale 2024" program (mini-grant 1.05.24.07.01). AJB acknowledges funding from the "First-Galaxies" Advanced Grant from the European Research Council (ERC) under the European Union's Horizon 2020 research and innovation program (Grant agreement No. 789056). SC and GV acknowledge support by European Union's HE ERC Starting Grant No. 101040227 – WINGS. KI acknowledges support from the National Natural Science Foundation of China (12573015, W2532003), the Beijing Natural Science Foundation (IS25003), and the China Manned Space Program (CMS-CSST-2025-A09). BL acknowledges the funding of the Deutsche Forschungsgemeinschaft (DFG, German Research Foundation) under Germany's Excellence Strategy EXC 2181/1 – 390900948 (the Heidelberg STRUCTURES Excellence Cluster). MP acknowledges support through the grants PID2021-127718NB-I00, PID2024-159902NA-I00, and RYC2023-044853-I, funded by the Spain Ministry of Science and Innovation/State Agency of Research MCIN/AEI/10.13039/501100011033 and El Fondo Social Europeo Plus FSE+. BRP acknowledges support from grants PID2021-127718NB-I00 and PID2024-158856NA-I00 funded by Spanish Ministerio de Ciencia e Innovación MCIN/AEI/10.13039/501100011033 and by "ERDF A way of making Europe". RS acknowledges support from the PRIN 2022 MUR project 2022CB3PJ3 "First Light And Galaxy aSsembly (FLAGS) funded by the European Union" Next Generation EU, and from EU-Recovery Fund PNRR – National Centre for HPC, Big Data and Quantum Computing. DS acknowledges support from the STFC, grant code ST/W000997/1. RV and AT acknowledge support from PRIN MUR "2022935STW" funded by European Union-Next Generation EU, Missione 4 Componente 2 CUP C53D23000950006 and from the Bando Ricerca Fondamentale INAF 2023, Theory Grant "Theoretical models for Black Holes Archaeology". SZ acknowledges the Texas Advanced Computing Center (TACC) for providing HPC resources under allocation AST23026. Views and opinions expressed are those of the authors only and do not necessarily reflect those of the European Union or the European Research Council Executive Agency. Neither the European Union nor the granting authority can be held responsible for them. This work is based on observations made with the NASA/ESA/CSA *James Webb* Space Telescope. The data were obtained from the Mikulski Archive for Space Telescopes at the Space Telescope Science Institute, which is operated by the Association of Universities for Research in Astronomy, Inc., under NASA contract NAS 5-03127 for JWST. These observations are associated with programs #1243 and #5015 (DOI:10.17909/5rh4-pa55).

References

Abuter, R., Allouche, F., Amorim, A., et al. 2024, Nature, 627, 281
Agazie, G., Anumarlapudi, A., Archibald, A. M., et al. 2023, ApJ, 952, L37
Agazie, G., Antoniadis, J., Anumarlapudi, A., et al. 2024, ApJ, 966, 105
Akins, H. B., Casey, C. M., Berg, D. A., et al. 2025, ApJ, 980, L29
Allen, M. G., Groves, B. A., Dopita, M. A., Sutherland, R. S., & Kewley, L. J. 2008, ApJS, 178, 20
Amaro-Seoane, P., Andrews, J., Arca Sedda, M., et al. 2023, Liv. Rev. Relat., 26, 2
Arevalo-Gonzalez, F., Braun, T., Trussler, J., et al. 2025, MNRAS, 544, 2737
Arribas, S., Perna, M., Rodríguez Del Pino, B., et al. 2024, A&A, 688, A146
Baes, M., Verstappen, J., De Looze, I., et al. 2011, ApJS, 196, 22
Bailey, J. A. 1998, SPIE Conf. Ser., 3355, 932
Baldwin, J. A., Phillips, M. M., & Terlevich, R. 1981, PASP, 93, 5
Beckers, J. M. 1982, Opt. Acta, 29, 361
Begelman, M. C., Blandford, R. D., & Rees, M. J. 1980, Nature, 287, 307
Bekenstein, J. D. 1973, ApJ, 183, 657
Bennert, V. N., Treu, T., Auger, M. W., et al. 2015, ApJ, 809, 20
Bennert, V. N., Loveland, D., Donohue, E., et al. 2018, MNRAS, 481, 138
Bennert, V. N., Treu, T., Ding, X., et al. 2021, ApJ, 921, 36
Bentz, M. C., Denney, K. D., Grier, C. J., et al. 2013, ApJ, 767, 149
Bertola, E., Cresci, G., Venturi, G., et al. 2025, A&A, 699, A220
Bezanson, R., van der Wel, A., Straatman, C., et al. 2018, ApJ, 868, L36
Bhowmick, A. K., Blecha, L., Kelley, L. Z., et al. 2025, ApJ, 991, 81
Binney, J., & Tremaine, S. 2008, Galactic Dynamics: Second Edition (Princeton University Press)
Blaes, O., Lee, M. H., & Socrates, A. 2002, ApJ, 578, 775
Blecha, L., Sijacki, D., Kelley, L. Z., et al. 2016, MNRAS, 456, 961
Blumenthal, K. A., & Barnes, J. E. 2018, MNRAS, 479, 3952
Böker, T., Arribas, S., Lützgendorf, N., et al. 2022, A&A, 661, A82
Bonetti, M., Haardt, F., Sesana, A., & Barausse, E. 2018, MNRAS, 477, 3910
Bonetti, M., Sesana, A., Haardt, F., Barausse, E., & Colpi, M. 2019, MNRAS, 486, 4044
Bongiorno, A., Merloni, A., Brusa, M., et al. 2012, MNRAS, 427, 3103
Boquien, M., Burgarella, D., Roehlly, Y., et al. 2019, A&A, 622, A103
Bourne, M. A., Fiacconi, D., Sijacki, D., Piotrowska, J. M., & Koudmani, S. 2024, MNRAS, 534, 3448
Brazzini, M., D'Eugenio, F., Maiolino, R., et al. 2025, MNRAS, 544, L167
Bruzual, G., & Charlot, S. 2003, MNRAS, 344, 1000
Buttigieg, S., Sijacki, D., Moore, C. J., & Bourne, M. A. 2025, MNRAS, 542, 2019
Calzetti, D., Armus, L., Bohlin, R. C., et al. 2000, ApJ, 533, 682
Camps, P., & Baes, M. 2015, Astron. Comput., 9, 20
Capelo, P. R., Volonteri, M., Dotti, M., et al. 2015, MNRAS, 447, 2123
Cappellari, M., Bacon, R., Bureau, M., et al. 2006, MNRAS, 366, 1126
Carniani, S., Venturi, G., Parlanti, E., et al. 2024, A&A, 685, A99
Chabrier, G. 2003, PASP, 115, 763
Chandrasekhar, S. 1943, ApJ, 97, 255
Chang, S.-J., Gronke, M., Matthee, J., & Mason, C. 2026, MNRAS, 545, staf2131
Charlot, S., & Fall, S. M. 2000, ApJ, 539, 718
Chen, C.-H., Ho, L. C., Li, R., & Zhuang, M.-Y. 2025, ApJ, 983, 60
Choe, S., Emil Rivera-Thorsen, T., Dahle, H., et al. 2025, A&A, 698, A16
Colpi, M., Possenti, A., & Gualandris, A. 2002, ApJ, 570, L85
Comerford, J. M., & Greene, J. E. 2014, ApJ, 789, 112
Comerford, J. M., Griffith, R. L., Gerke, B. F., et al. 2009, ApJ, 702, L82
Comerford, J. M., Schluns, K., Greene, J. E., & Cool, R. J. 2013, ApJ, 777, 64
Comerford, J. M., Pooley, D., Barrows, R. S., et al. 2015, ApJ, 806, 219
Concas, A., Maiolino, R., Curti, M., et al. 2022, MNRAS, 513, 2535
Crenshaw, D. M., Peterson, B. M., & Wagner, R. M. 1988, AJ, 96, 1208
Cresci, G., Tozzi, G., Perna, M., et al. 2023, A&A, 672, A128
Curti, M., Cataldi, E., Belfiore, F., et al. 2026, A&A, 710, A18
Dale, D. A., Helou, G., Magdis, G. E., et al. 2014, ApJ, 784, 83
Dalmasso, N., Calabrò, A., Leethochawalit, N., et al. 2024, MNRAS, 533, 4472
de Nicola, S., Thomas, J., Saglia, R. P., et al. 2025, ApJ, submitted [arXiv:2512.04178]
Deane, R. P., Paragi, Z., Jarvis, M. J., et al. 2014, Nature, 511, 57
D'Eugenio, F., Pérez-González, P. G., Maiolino, R., et al. 2024, Nat. Astron., 8, 1443
D'Eugenio, F., Juodžbalis, I., Ji, X., et al. 2026a, MNRAS, 545, staf2117
D'Eugenio, F., Maiolino, R., Perna, M., et al. 2026b, MNRAS, 547, stag401
Di Matteo, T., Springel, V., & Hernquist, L. 2005, Nature, 433, 604
Dong-Páez, C. A., Volonteri, M., Dubois, Y., Beckmann, R. S., & Trebitsch, M. 2025, A&A, 695, A231
Draine, B. T. 2011, Physics of the Interstellar and Intergalactic Medium
Duan, Q., Conselice, C. J., Li, Q., et al. 2025, MNRAS, 540, 774
Dubois, Y., Volonteri, M., & Silk, J. 2014, MNRAS, 440, 1590
Duffell, P. C., D'Orazio, D., Derdzinski, A., et al. 2020, ApJ, 901, 25
Dupletsa, U., Harms, J., Banerjee, B., et al. 2023, Astron. Comput., 42, 100671
Eisenstein, D. J., Willott, C., Alberts, S., et al. 2026, ApJS, 283, 6
EPTA Collaboration, InPTA Collaboration, Antoniadis, J., et al. 2024, A&A, 690, A118
Faisst, A. L., Fujimoto, S., Tsujita, A., et al. 2026, ApJS, 282, 19
Farris, B. D., Duffell, P., MacFadyen, A. I., & Haiman, Z. 2014, ApJ, 783, 134
Ferland, G. J., Porter, R. L., van Hoof, P. A. M., et al. 2013, Rev. Mex. Astron. Astrofis., 49, 137
Ferrarese, L., & Ford, H. 2005, Space Sci. Rev., 116, 523
Ferrarese, L., & Merritt, D. 2000, ApJ, 539, L9
Ficarra, G., Ciarfella, A., & Lousto, C. O. 2023, Phys. Rev. D, 108, 064045

Förster Schreiber, N. M., Übler, H., Davies, R. L., et al. 2019, ApJ, 875, 21
Fries, L. B., Trump, J. R., Horne, K., et al. 2024, ApJ, 975, 239
Furtak, L. J., Labbé, I., Zitrin, A., et al. 2024, Nature, 628, 57
Gaia Collaboration (Brown, A. G. A., et al.) 2018, A&A, 616, A1
Gal-Yam, A. 2012, Science, 337, 927
García-Quirós, C., Colleoni, M., Husa, S., et al. 2020, Phys. Rev. D, 102, 064002
Geris, S., Maiolino, R., Isobe, Y., et al. 2026, MNRAS, 545, staf1979
Gnerucci, A., Marconi, A., Capetti, A., Axon, D. J., & Robinson, A. 2010, A&A, 511, A19
Gordon, K. D., Clayton, G. C., Misselt, K. A., Landolt, A. U., & Wolff, M. J. 2003, ApJ, 594, 279
Grandi, S. A. 1975, ApJ, 196, 465
Grandi, S. A. 1980, ApJ, 238, 10
GRAVITY Collaboration (Amorim, A., et al.) 2024, A&A, 684, A167
GRAVITY+ Collaboration (Abd El Dayem, K., et al.) 2026, A&A, 706, A99
Green, P. J., Myers, A. D., Barkhouse, W. A., et al. 2010, ApJ, 710, 1578
Greene, J. E., & Ho, L. C. 2005, ApJ, 630, 122
Greene, J. E., Strader, J., & Ho, L. C. 2020, ARA&A, 58, 257
Greene, J. E., Labbe, I., Goulding, A. D., et al. 2024, ApJ, 964, 39
Greene, J. E., Setton, D. J., Furtak, L. J., et al. 2026, ApJ, 996, 129
Gutiérrez, C. P., Anderson, J. P., Hamuy, M., et al. 2017, ApJ, 850, 89
Habouzit, M. 2025, MNRAS, 537, 2323
Habouzit, M., Onoue, M., Bañados, E., et al. 2022, MNRAS, 511, 3751
Hanawa, T., Ochi, Y., & Ando, K. 2010, ApJ, 708, 485
Harikane, Y., Zhang, Y., Nakajima, K., et al. 2023, ApJ, 959, 39
Harrison, C. M., Alexander, D. M., Mullaney, J. R., et al. 2016, MNRAS, 456, 1195
Hills, J. G., & Fullerton, L. W. 1980, AJ, 85, 1281
Hirschmann, M., Khochfar, S., Burkert, A., et al. 2010, MNRAS, 407, 1016
Hirschmann, M., Charlot, S., Feltre, A., et al. 2019, MNRAS, 487, 333
Ho, L. C., & Kim, M. 2014, ApJ, 789, 17
Hoffman, L., & Loeb, A. 2007, MNRAS, 377, 957
Hopkins, P. F., Hernquist, L., Cox, T. J., & Kereš, D. 2008, ApJS, 175, 356
Husemann, B., Worseck, G., Arrigoni Battaia, F., & Shanks, T. 2018, A&A, 610, L7
Ilić, D., Popović, L. Č., La Mura, G., Ciroi, S., & Rafanelli, P. 2012, A&A, 543, A142
Inayoshi, K., Kimura, S. S., & Noda, H. 2025, PASJ, 77, 811
Izotov, Y. I., Guseva, N. G., Fricke, K. J., et al. 2010, A&A, 517, A90
Jahnke, K., & Macciò, A. V. 2011, ApJ, 734, 92
Jakobsen, P., Ferruit, P., Alves de Oliveira, C., et al. 2022, A&A, 661, A80
Jeon, J., Liu, B., Bromm, V., & Finkelstein, S. L. 2023, MNRAS, 524, 176
Ji, X., Maiolino, R., Übler, H., et al. 2025, MNRAS, 544, 3900
Ji, X., D'Eugenio, F., Juodžbalis, I., et al. 2026, MNRAS, 545, staf2235
Jiang, L., Fan, X., Vestergaard, M., et al. 2007, AJ, 134, 1150
Johansson, P. H., Naab, T., & Burkert, A. 2009, ApJ, 690, 802
Jones, G. C., Übler, H., Perna, M., et al. 2024, A&A, 682, A122
Jones, G. C., Bowler, R. A. A., Bunker, A. J., et al. 2026a, MNRAS, 547, stag336
Jones, G. C., Übler, H., Maiolino, R., et al. 2026b, MNRAS, 546, stag115
Junkkarinen, V., Shields, G. A., Beaver, E. A., et al. 2001, ApJ, 549, L155
Juodžbalis, I., Ji, X., Maiolino, R., et al. 2024a, MNRAS, 535, 853
Juodžbalis, I., Maiolino, R., Baker, W. M., et al. 2024b, Nature, 636, 594
Juodžbalis, I., Maiolino, R., Baker, W. M., et al. 2026a, MNRAS, 546, stag086
Juodžbalis, I., Marconcini, C., D'Eugenio, F., et al. 2026b, Nature, 653, 1017
Kashino, D., Lilly, S. J., Matthee, J., et al. 2023, ApJ, 950, 66
Kaspi, S., Smith, P. S., Netzer, H., et al. 2000, ApJ, 533, 631
Kauffmann, G., & Haehnelt, M. 2000, MNRAS, 311, 576
Kewley, L. J., Dopita, M. A., Leitherer, C., et al. 2013a, ApJ, 774, 100
Kewley, L. J., Maier, C., Yabe, K., et al. 2013b, ApJ, 774, L10
Khan, F. M., Fiacconi, D., Mayer, L., Berczik, P., & Just, A. 2016, ApJ, 828, 73
Kocevski, D. D., Onoue, M., Inayoshi, K., et al. 2023, ApJ, 954, L4
Kokorev, V., Fujimoto, S., Labbe, I., et al. 2023, ApJ, 957, L7
Kollatschny, W., & Zetzl, M. 2011, Nature, 470, 366
Kollatschny, W., & Zetzl, M. 2013, A&A, 549, A100
Kollatschny, W., Weilbacher, P. M., Ochmann, M. W., et al. 2020, A&A, 633, A79
Komossa, S., Burwitz, V., Hasinger, G., et al. 2003, ApJ, 582, L15
Kormendy, J., & Gebhardt, K. 2001, AIP Conf. Ser., 586, 363
Kormendy, J., & Ho, L. C. 2013, ARA&A, 51, 511
Koss, M. J., Treister, E., Kakkad, D., et al. 2023, ApJ, 942, L24
Kulier, A., Ostriker, J. P., Natarajan, P., Lackner, C. N., & Cen, R. 2015, ApJ, 799, 178
Kulkarni, G., & Loeb, A. 2012, MNRAS, 422, 1306
Kurk, J. D., Walter, F., Fan, X., et al. 2007, ApJ, 669, 32
La Mura, G., Popović, L. Č., Ciroi, S., Rafanelli, P., & Ilić, D. 2007, ApJ, 671, 104
Labbe, I., Greene, J. E., Matthee, J., et al. 2024, ApJ, submitted [arXiv:2412.04557]
Lambrides, E., Larson, R. L., Garofali, K., et al. 2026, Nat. Astron. [arXiv:2409.13047]
Lamperti, I., Arribas, S., Perna, M., et al. 2024, A&A, 691, A153
Li, J., Silverman, J. D., Shen, Y., et al. 2025, ApJ, 981, 19
Li, R., Ho, L. C., & Chen, C.-H. 2026, ApJ, 999, 70
Liao, S., Irodotou, D., Johansson, P. H., et al. 2024, MNRAS, 528, 5080
Lin, X., Fan, X., Cai, Z., et al. 2026a, ApJ, 997, 364
Lin, X., Fan, X., Wang, F., et al. 2026b, ApJ, 996, 93
Liu, H., & Inayoshi, K. 2025, Phys. Rev. D, 111, 043012
Liu, X., Hou, M., Li, Z., et al. 2019, ApJ, 887, 90
Loiacono, F., Gilli, R., Mignoli, M., et al. 2025, A&A, 703, A36
López, I. E., Brusa, M., Bonoli, S., et al. 2023, A&A, 672, A137
Lu, K.-X., Bai, J.-M., Wang, J.-M., et al. 2022, ApJS, 263, 10
Lupi, A., Haiman, Z., & Volonteri, M. 2021, MNRAS, 503, 5046
Lupi, A., Trinca, A., Volonteri, M., Dotti, M., & Mazzucchelli, C. 2024, A&A, 689, A128
Ma, Y., Greene, J. E., Setton, D. J., et al. 2026, ApJ, 1000, 59
Madau, P., & Quataert, E. 2004, ApJ, 606, L17
Maiolino, R., Scholtz, J., Curtis-Lake, E., et al. 2024a, A&A, 691, A145
Maiolino, R., Scholtz, J., Witstok, J., et al. 2024b, Nature, 627, 59
Maiolino, R., Risaliti, G., Signorini, M., et al. 2025, MNRAS, 538, 1921
Maiolino, R., Übler, H., D'Eugenio, F., et al. 2026, MNRAS, 548, staf2109
Mannerkoski, M., Johansson, P. H., Rantala, A., Naab, T., & Liao, S. 2021, ApJ, 912, L20
Mannerkoski, M., Johansson, P. H., Rantala, A., et al. 2022, ApJ, 929, 167
Mannucci, F., Pancino, E., Belfiore, F., et al. 2022, Nat. Astron., 6, 1185
Marconi, A., Axon, D. J., Maiolino, R., et al. 2008, ApJ, 678, 693
Marshall, M. A., Yue, M., Eilers, A.-C., et al. 2025, A&A, 702, A50
Martins, F., Schaerer, D., Haemmerlé, L., & Charbonnel, C. 2020, A&A, 633, A9
Matsuoka, Y., Kawara, K., & Oyabu, S. 2008, ApJ, 673, 62
Matsuoka, Y., Izumi, T., Onoue, M., et al. 2024, ApJ, 965, L4
Matthee, J., Naidu, R. P., Brammer, G., et al. 2024, ApJ, 963, 129
Mayer, L., Kazantzidis, S., Madau, P., et al. 2007, Science, 316, 1874
Mazzolari, G., Übler, H., Maiolino, R., et al. 2024, A&A, 691, A345
Mazzolari, G., Scholtz, J., Maiolino, R., et al. 2025, A&A, 700, A12
McClymont, W., Tacchella, S., Ji, X., et al. 2026, MNRAS, 545, staf2092
McConnell, N. J., & Ma, C.-P. 2013, ApJ, 764, 184
Menou, K., Haiman, Z., & Narayanan, V. K. 2001, ApJ, 558, 535
Mérida, R. M., Gaspar, G., Sawicki, M., et al. 2025, A&A, 698, A317
Merritt, D., Milosavljević, M., Favata, M., Hughes, S. A., & Holz, D. E. 2004, ApJ, 607, L9
Mezcua, M., Siudek, M., Suh, H., et al. 2023, ApJ, 943, L5
Mezcua, M., Pacucci, F., Suh, H., Siudek, M., & Natarajan, P. 2024, ApJ, 966, L30
Mikkola, S., & Valtonen, M. J. 1990, ApJ, 348, 412
Morgan, L. A. 1971, MNRAS, 153, 393
Mountrichas, G., Masoura, V. A., Xilouris, E. M., et al. 2022, A&A, 661, A108
Münch, G., & Taylor, K. 1974, ApJ, 192, L93
Naidu, R. P., Matthee, J., Katz, H., et al. 2025, ArXiv e-prints [arXiv:2503.16596]
Nakajima, K., & Maiolino, R. 2022, MNRAS, 513, 5134
Natarajan, P., Pacucci, F., Ricarte, A., et al. 2024, ApJ, 960, L1
Netzer, H. 2019, MNRAS, 488, 5185
Netzer, H., & Penston, M. V. 1976, MNRAS, 174, 319
Neureiter, B., Thomas, J., Rantala, A., et al. 2023, ApJ, 950, 15
Neuschaefer, L. W., & Windhorst, R. A. 1995, ApJS, 96, 371
Ochi, Y., Sugimoto, K., & Hanawa, T. 2005, ApJ, 623, 922
O'Leary, R. M., & Loeb, A. 2009, MNRAS, 395, 781
Osterbrock, D. E. 1977, ApJ, 215, 733
Osterbrock, D. E. 1981, ApJ, 249, 462
Osterbrock, D. E., & Ferland, G. J. 2006, Astrophysics of Gaseous Nebulae and Active Galactic Nuclei
Ostriker, E. C. 1999, ApJ, 513, 252
Ostriker, J. P., & Tremaine, S. D. 1975, ApJ, 202, L113
Pacucci, F., & Loeb, A. 2020, ApJ, 895, 95
Padovani, P., Alexander, D. M., Assef, R. J., et al. 2017, A&ARv, 25, 2
Parlanti, E., Carniani, S., Übler, H., et al. 2024, A&A, 684, A24
Parlanti, E., Carniani, S., Venturi, G., et al. 2025a, A&A, 695, A6
Parlanti, E., Trefoloni, B., Carniani, S., et al. 2025b, A&A, in press [arXiv:2512.14844]
Partmann, C., Naab, T., Rantala, A., et al. 2024, MNRAS, 532, 4681
Pastorello, A., Turatto, M., Benetti, S., et al. 2002, MNRAS, 333, 27
Peres, A. 1962, Phys. Rev., 128, 2471
Perna, M., Arribas, S., Catalán-Torrecilla, C., et al. 2020, A&A, 643, A139
Perna, M., Arribas, S., Marshall, M., et al. 2023, A&A, 679, A89
Perna, M., Arribas, S., Costantin, L., et al. 2025a, A&A, submitted [arXiv:2512.14874]

Perna, M., Arribas, S., Lamperti, I., et al. 2025b, A&A, 696, A59
Peters, P. C. 1964, Phys. Rev., 136, 1224
Peters, P. C., & Mathews, J. 1963, Phys. Rev., 131, 435
Peterson, B. M., Berlind, P., Bertram, R., et al. 2002, ApJ, 581, 197
Pfeifle, R. W., Satyapal, S., Manzano-King, C., et al. 2019, ApJ, 883, 167
Piana, O., Dayal, P., Volonteri, M., & Choudhury, T. R. 2021, MNRAS, 500, 2146
Puglisi, A., Rodighiero, G., Franceschini, A., et al. 2016, A&A, 586, A83
Puskás, D., Tacchella, S., Simmonds, C., et al. 2025, MNRAS, 540, 2146
Quinlan, G. D. 1996, New Astron., 1, 35
Rantala, A., Pihajoki, P., Johansson, P. H., et al. 2017, ApJ, 840, 53
Rantala, A., Lahén, N., Naab, T., Escobar, G. J., & Iorio, G. 2025, MNRAS, 543, 2130
Rawlings, A., Johansson, P. H., Naab, T., et al. 2025, ApJ, 991, 83
Regan, J., & Volonteri, M. 2024, Open J. Astrophys., 7, 72
Reines, A. E., & Volonteri, M. 2015, ApJ, 813, 82
Reines, A. E., Greene, J. E., & Geha, M. 2013, ApJ, 775, 116
Remigio, R. P., U, V., Barth, A. J., et al. 2025, ApJ, 992, 42
Ren, W., Silverman, J. D., Faisst, A. L., et al. 2025, MNRAS, 544, 211
Richards, G. T., Lacy, M., Storrie-Lombardi, L. J., et al. 2006, ApJS, 166, 470
Rigamonti, F., Severgnini, P., Sottocorno, E., et al. 2025, A&A, 693, A117
Rinaldi, P., Pérez-González, P. G., Rieke, G. H., et al. 2025, ApJ, 994, 86
Rodríguez-Ardila, A., Viegas, S. M., Pastoriza, M. G., Prato, L., & Donzelli, C. J. 2002, ApJ, 572, 94
Rosborough, S. A., Robinson, A., Almeyda, T., Humphrey, D., & Noll, M. 2025, ApJ, 991, 143
Rusakov, V., Watson, D., Nikopoulos, G. P., et al. 2026, Nature, 649, 574
Ryu, T., Perna, R., Haiman, Z., Ostriker, J. P., & Stone, N. C. 2018, MNRAS, 473, 3410
Saeedzadeh, V., Babul, A., Mukherjee, S., et al. 2024, ApJ, 975, 265
Saglia, R., Mehrgan, K., de Nicola, S., et al. 2024, A&A, 692, A124
Saslaw, W. C., Valtonen, M. J., & Aarseth, S. J. 1974, ApJ, 190, 253
Sayeb, M., Blecha, L., & Kelley, L. Z. 2024, MNRAS, 527, 7424
Schartmann, M., Meisenheimer, K., Camenzind, M., Wolf, S., & Henning, T. 2005, A&A, 437, 861
Schneider, R., Valiante, R., Trinca, A., et al. 2023, MNRAS, 526, 3250
Scholtz, J., Maiolino, R., D'Eugenio, F., et al. 2025, A&A, 697, A175
Scialpi, M., Mannucci, F., Marconcini, C., et al. 2024, A&A, 690, A57
Shapley, A. E., Sanders, R. L., Topping, M. W., et al. 2025, ApJ, 980, 242
Shields, G. A., Oke, J. B., & Sargent, W. L. W. 1972, ApJ, 176, 75
Sijacki, D., Springel, V., Di Matteo, T., & Hernquist, L. 2007, MNRAS, 380, 877
Sijacki, D., Springel, V., & Haehnelt, M. G. 2011, MNRAS, 414, 3656
Sijacki, D., Vogelsberger, M., Genel, S., et al. 2015, MNRAS, 452, 575
Silverman, J. D., Li, J., Ding, X., et al. 2025, ApJ, 995, L67
Siwek, M., Weinberger, R., Muñoz, D. J., & Hernquist, L. 2023, MNRAS, 518, 5059
Soltan, A. 1982, MNRAS, 200, 115
Springel, V., Di Matteo, T., & Hernquist, L. 2005, ApJ, 620, L79
Stalevski, M., Ricci, C., Ueda, Y., et al. 2016, MNRAS, 458, 2288
Steinborn, L. K., Dolag, K., Comerford, J. M., et al. 2016, MNRAS, 458, 1013
Stern, J., & Laor, A. 2012, MNRAS, 423, 600
Storchi-Bergmann, T., Schimoia, J. S., Peterson, B. M., et al. 2017, ApJ, 835, 236
Strom, A. L., Rudie, G. C., Trainor, R. F., et al. 2023, ApJ, 958, L11
Sutherland, R., Dopita, M., Binette, L., & Groves, B. 2018, Astrophysics Source Code Library [record ascl:1807.005]
Taddia, F., Stritzinger, M. D., Sollerman, J., et al. 2013, A&A, 555, A10
Talbot, R. Y., Sijacki, D., & Bourne, M. A. 2024, MNRAS, 528, 5432
Tanaka, T., & Haiman, Z. 2009, ApJ, 696, 1798
Tanaka, T. S., Silverman, J. D., Shimasaku, K., et al. 2024, ArXiv e-prints [arXiv:2412.14246]
Taylor, A. J., Kokorev, V., Kocevski, D. D., et al. 2025, ApJ, 989, L7
Thorne, K. S., & Braginskii, V. B. 1976, ApJ, 204, L1
Torralba, A., Matthee, J., Pezzulli, G., et al. 2026, A&A, 707, A75
Trakhtenbrot, B., Volonteri, M., & Natarajan, P. 2017, ApJ, 836, L1
Tremmel, M., Karcher, M., Governato, F., et al. 2017, MNRAS, 470, 1121
Tripodi, R., Bradač, M., D'Eugenio, F., et al. 2025a, ApJ, 994, L6
Tripodi, R., Martis, N., Markov, V., et al. 2025b, Nat. Commun., 16, 9830
Übler, H., Maiolino, R., Curtis-Lake, E., et al. 2023, A&A, 677, A145
Übler, H., D'Eugenio, F., Perna, M., et al. 2024a, MNRAS, 533, 4287
Übler, H., Maiolino, R., Pérez-González, P. G., et al. 2024b, MNRAS, 531, 355
Ulivi, L., Mannucci, F., Scialpi, M., et al. 2025, A&A, submitted [arXiv:2508.19494]
Valiante, R., Colpi, M., Schneider, R., et al. 2021, MNRAS, 500, 4095
van der Wel, A., van Houdt, J., Bezanson, R., et al. 2022, ApJ, 936, 9
Van Wassenhove, S., Volonteri, M., Mayer, L., et al. 2012, ApJ, 748, L7
Veilleux, S., & Osterbrock, D. E. 1987, ApJS, 63, 295
Venturi, G., Carniani, S., Bertola, E., et al. 2026, A&A, in press, https://doi.org/10.1051/0004-6361/202558509
Volonteri, M., Haardt, F., & Madau, P. 2003, ApJ, 582, 559
Volonteri, M., Pfister, H., Beckmann, R. S., et al. 2020, MNRAS, 498, 2219
Volonteri, M., Pfister, H., Beckmann, R., et al. 2022, MNRAS, 514, 640
Wang, B., Leja, J., de Graaff, A., et al. 2024, ApJ, 969, L13
Willott, C. J., McLure, R. J., & Jarvis, M. J. 2003, ApJ, 587, L15
Willott, C. J., Albert, L., Arzoumanian, D., et al. 2010, AJ, 140, 546
Yang, G., Boquien, M., Buat, V., et al. 2020, MNRAS, 491, 740
Yang, G., Caputi, K. I., Papovich, C., et al. 2023, ApJ, 950, L5
Yu, Q. 2002, MNRAS, 331, 935
Zamora, S., Venturi, G., Carniani, S., et al. 2025, A&A, 702, A102
Zhang, S., Bromm, V., & Liu, B. 2024, ApJ, 975, 139
Zhang, J., Egami, E., Sun, F., et al. 2026, ApJ, 997, 250

[1] Max-Planck-Institut für extraterrestrische Physik, Gießenbachstraße 1, 85748 Garching, Germany
[2] Kavli Institute for Cosmology, University of Cambridge, Madingley Road, Cambridge CB3 0HA, UK
[3] Cavendish Laboratory, University of Cambridge, 19 JJ Thomson Avenue, Cambridge CB3 0HE, UK
[4] Department of Physics and Astronomy, University College London, Gower Street, London WC1E 6BT, UK
[5] INAF/Osservatorio Astronomico di Roma, Via Frascati 33, 00040 Monte Porzio Catone, Italy
[6] Centro de Astrobiología (CAB), CSIC-INTA, Ctra. de Ajalvir km 4, Torrejón de Ardoz E-28850, Madrid, Spain
[7] Institute of Science and Technology Austria (ISTA), Am Campus 1, 3400 Klosterneuburg, Austria
[8] Dipartimento di Fisica, Sapienza Università di Roma, P.le A. Moro 2, 00185 Roma, Italy
[9] INAF – Osservatorio Astrofisco di Arcetri, largo E. Fermi 5, 50127 Firenze, Italy
[10] Department of Physics, University of Oxford, Denys Wilkinson Building, Keble Road, Oxford OX13RH, UK
[11] Department of Astronomy, University of Texas, Austin, TX 78712, USA
[12] Scuola Normale Superiore, Piazza dei Cavalieri 7, I-56126 Pisa, Italy
[13] Sorbonne Université, CNRS, UMR 7095, Institut d'Astrophysique de Paris, 98 bis bd Arago, 75014 Paris, France
[14] European Southern Observatory, Karl-Schwarzschild-Strasse 2, 85748 Garching, Germany
[15] Department of Physics, TUM School of Natural Sciences, Technical University of Munich, 85748 Garching, Germany
[16] Institute of Astronomy, Madingley Road, Cambridge CB3 0HA, UK
[17] Departments of Physics and Astronomy, University of California, Berkeley, CA 94720, USA
[18] Kavli Institute for Astronomy and Astrophysics, Peking University, Beijing 100871, China
[19] Universität Heidelberg, Zentrum für Astronomie, Institut für Theoretische Astrophysik, Albert Ueberle Str. 2, D-69120 Heidelberg, Germany
[20] National Astronomical Observatory of Japan (NAOJ), 2-21-1, Osawa, Mitaka, Tokyo 181-8588, Japan
[21] Department of Physics, ETH Zürich, Wolfgang-Pauli-Strasse 27, Zürich 8093, Switzerland
[22] Institute of Physics, Laboratory of Astrophysics, Ecole Polytechnique Fédérale de Lausanne (EPFL), Observatoire de Sauverny, 1290 Versoix, Switzerland
[23] Department of Astronomy and Astrophysics, University of California, Santa Cruz, 1156 High Street, Santa Cruz, CA 95064, USA
[24] Como Lake Center for Astrophysiscs, DiSAT Università degli Studi dell'Insubria, Via Valleggio 11, 22100 Como, Italy
[25] NRC Herzberg, 5071 West Saanich Rd, Victoria BC V9E 2E7, Canada
[26] Department of Physics, University of Texas at Austin, Austin, TX 78712, USA
[27] Weinberg Institute for Theoretical Physics, Texas Center for Cosmology and Astroparticle Physics, University of Texas at Austin, Austin, TX 78712, USA

Appendix A: Full $R \sim 2700$ spectrum of the main galaxy

In Fig. A.1 we show the full high-resolution spectrum integrated within the main galaxy aperture (without continuum subtraction). The locations of several emission lines discussed in Sect. 3 are indicated; we mask the detector gap where fewer than 15 slices contribute to the emission ($\lambda_{\rm gap} \sim 4.03 - 4.16\mu$m). The continuum is not or only marginally detected in the high-resolution data.

Appendix B: Channel maps of BLR1 and BLR2

In Fig. B.1 we show the channel maps obtained for BLR1 and BLR2 as describe in Sect. 3.1. The flux distributions of BLR1 and BLR2 are distinct, indicating that they do not originate from the same point source.

As described in Sect. 3, we determine the centroids of BLR1 and BLR2 through two-dimensional Gaussian fits to the flux distribution of the two maps. Uncertainties are derived by varying the input images 10000 times each with their associated noise, repeating the fits, and adopting half the 68th percentile of the distribution as the uncertainties. The corresponding positions together with twice their fit uncertainty are indicated as a teal cross (BLR1) and a brown plus (BLR2) in Fig. B.1. We find positional uncertainties of 0.07 and 0.09 pixels. In general, the centroid of a point source can be determined with a precision of $\delta_{x,y} \sim 0.4 \cdot {\rm FWHM}/(S/N)$, where S/N is measured at the peak (e.g. Neuschaefer & Windhorst 1995). In our case, we find $S/N \sim 17$ and $S/N \sim 11$ for the brightest $0.05'' \times 0.05''$ pixel of BLR1 and BLR2, indicating $\delta_{x,y} \sim 0.09$ and ~ 0.14 pixels, respectively. However, due to sampling several pixels contribute to the peak and the true S/N and precision is expected to be better. From the centroid measurements, we calculate the projected distance of BLR1 and BLR2 and find $d_{\rm I,II} = 190 \pm 40$. In Appendix C we demonstrate through mock tests that this distance and associated uncertainty are realistic, although the uncertainty may be underestimated by 10 – 20 pc. We further note that, assuming the theoretically derived (upper limit) uncertainties on the positional measurements, we find a distance uncertainty of 50 pc.

The FWHM we determine from the Gaussian fits to the images are compatible with the expected FWHM of a point source observed with NIRSpec at the wavelength of Hα (ca. $0.197''$, i.e. 3.94 pixel of $0.05''$): we find 4.24 ± 0.21 and 3.64 ± 0.73 pixels for the average FWHM of BLR1 and BLR2 from our fits, where again the uncertainties are derived from our Monte Carlo runs.

Appendix C: Mock tests concerning the separation of BLR1 and BLR2

In Sect. 3.1 we describe how we measure the projected separation of BLR1 and BLR2 from channel maps, finding $d_{\rm I,II} = 190 \pm 40$. To test whether such a positional uncertainty is reliable, we create two sets of 10000 two-dimensional Gaussians with a FWHM= $0.197''$(the PSF FWHM at the wavelength of Hα). This is to simulate the expected spread of a point-source (namely a BLR at cosmological distance) at the wavelength of Hα. The two sets of Gaussians are centred on the BLR1 and BLR2 centroids we measured from the channel maps in Sect. 3.1, respectively. We add random noise, corresponding to the levels we measure in the channel maps of BLR1 and BLR2, respectively. We then measure the centroids of the resulting maps from a two-dimensional Gaussian fit and derive their distances. We find a median distance of 200^{+60}_{-40} pc, where the uncertainties correspond to the 68$^{\rm th}$ confidence interval of the distribution. This suggests that the uncertainty of 40 pc on the projected distance of BLR1 and BLR2 we derived in Sect. 3.1 is plausible, although may be underestimated by 10 – 20 pc.

In Fig. C.1 we show the ratio after peak flux normalisation of two of these mock BLRs (i.e. corresponding to the right panel in Fig. 2). Like in the main part of the paper, we plot pixels with $S/N \geq 0.5$. The NE to SW pattern obtained is qualitatively similar to what we found from our data in Sect. 3.1. This further supports our interpretation that the two broad Hα components in the centre of J0148-4214 are indeed two point sources, separated by less than the PSF FWHM.

Appendix D: $R \sim 100$ fitting

The prism observations covering the wavelength range 0.6μm - 5.3μm reveal many additional emission lines in the regime not covered by our high-resolution data. We model narrow emission lines as Gaussians and tie the line centroids and narrow line widths for three groups of lines: (i) blue-wards of [O II]$_{3726,3729}$, (ii) from [OII] to [O III]$_{4959,5007}$, (iii) from He I$_{\lambda 5876}$ and red-wards. We also include one broad component for Hα and for Hβ (the resolution is too low to separate the two central BLRs spectrally). The continuum is modelled as a polynomial.

We show our fit to the main galaxy aperture spectrum in Fig. D.1 and list the best-fit emission line fluxes in Table D.1. We note the detection of O I$_{8446}$ in our prism aperture spectrum. This line has been detected in low-z Seyfert I, low-metallicity AGNs and quasars (e.g. Shields et al. 1972; Netzer & Penston 1976; Grandi 1980; Rodríguez-Ardila et al. 2002; Matsuoka et al. 2008; Izotov et al. 2010) as well as in galactic emission nebulae (e.g. Morgan 1971; Münch & Taylor 1974; Grandi 1975). At high redshifts, it has been detected in a stack of $z \sim 2 - 3$ star-forming galaxies from the CECILIA survey (Strom et al. 2023), in the Sunburst Arc (Choe et al. 2025), in a Wolf-Rayet galaxy from the MARTA survey (Curti et al. 2026), and in a few $z \sim 2 - 5$ AGNs (Juodžbalis et al. 2024a; Labbe et al. 2024; D'Eugenio et al. 2026a; Tripodi et al. 2025a). The line-strength of O I$_{8446}$ relative to Hα found for J0148-4214, O I$_{8446}$/H$\alpha_{\rm narrow} = 0.048$, O I$_{8446}$/H$\alpha_{\rm BLR} = 0.076$ and O I$_{8446}$/H$\alpha_{\rm total} = 0.029$ is comparable to those of local Seyfert I galaxies (assuming negligible contamination from Paschen 17 and 18), while for the CECILIA star-forming sample and the galaxy from the MARTA program a sub-percentage ratio is found.

We also note a clear change in strong emission line ratios and blue continuum slope across J0148-4214, seen to a lesser extent also in the high-resolution data. In Fig. D.2 we show two-by-two spaxel extractions north-east (brown) and south-west (teal) of the galaxy centre of the J0148-4214 prism data cube. Naturally, the extractions have lower S/N compared to our main galaxy aperture extraction shown in Fig. D.1, which is especially apparent in the rest-frame UV region. Despite this, the extracted regions clearly have different spectral slopes in the rest-frame UV. A change in the strong rest-frame optical emission line ratios is also evident. These differences could be explained through different excitation sources, such as two black holes, or could be the imprint of the small blue source closest to J0148-4214 which is seen in the NIRCam imaging. We defer a detailed analysis of the prism data and the continuum properties of J0148-4214 and its potential satellites to future work.

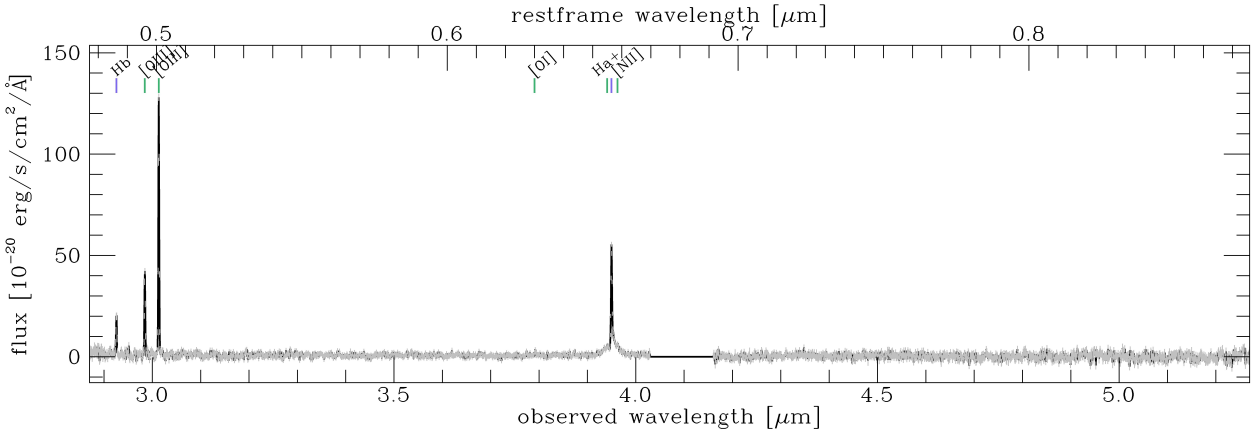

Fig. A.1. Full $R \sim 2700$ spectrum of the main galaxy (orange aperture in Fig. 1). We indicate the locations of several emission lines. The detector gap is masked in the region $\lambda_{\rm gap} \sim 4.03 - 4.16\mu$m, where fewer than 15 slices contribute to the emission.

Table D.1. $R\sim100$ emission line fluxes.

C IV$_{1546,1551}$	He II$_{1640}$	C III]$_{1909}$	[O II]$_{3726,3729}$	[Ne III]$_{3869}$	[Ne III]$_{3967}$	Hγ+[O III]$_{4363}$	H$\beta_{\rm narrow}$	[O III]$_{5007}$
6.2 ± 1.8	2.4 ± 1.2	1.8 ± 0.8	1.7 ± 0.2	2.3 ± 0.2	0.5 ± 0.2	1.4 ± 0.2	4.2 ± 0.5	28.5 ± 0.5
He I$_{5876}$	H$\alpha_{\rm narrow}$	H$\alpha_{\rm BLR}$	[N II]$_{6583}$	[S II]$_{6717,6731}$	He I$_{7065}$	O I$_{8446}$		log(EW$_{\rm He\ II}$)
1.0 ± 0.2	20.5 ± 1.0	12.9 ± 1.9	2.4 ± 1.1	0.6 ± 0.1	1.0 ± 0.2	1.0 ± 0.3		1.1 ± 0.5

Notes. Observed $R\sim100$ emission line fluxes with $S/N \gtrsim 2$ in units of 10^{-18} erg/s/cm^2 and the equivalent width of He II$_{1640}$ in Å, extracted from the region outlined in orange in Fig. 1, corresponding to the fit shown in Fig. D.1. Due to the lower resolution of the prism, the two broad Hα components, as well as several emission lines doublets and close pairs, are blended. Specifically, in addition to what is indicated below, [Ne III]$_{3869}$ is also blended with He I$_{3889}$ and [Ne III]$_{3967}$ would be blended with Hϵ, although in this case the contribution would be negligible.

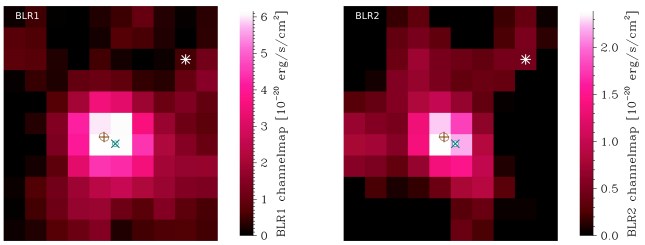

Fig. B.1. Channel maps of the two central broad Hα components, for BLR1 (*left*) and BLR2 (*right*), derived as described in Sect. 3.1. The centroids of the channel maps obtained from two-dimensional Gaussian fits are indicated as a teal cross and a brown plus for BLR1 and BLR2, respectively; the ellipses show two times the centroid uncertainty. The white star marks the position of the third BLR detected in J0148-4214. The flux distributions of BLR1 and BLR2 are distinct, indicating that they do not originate from the same point source.

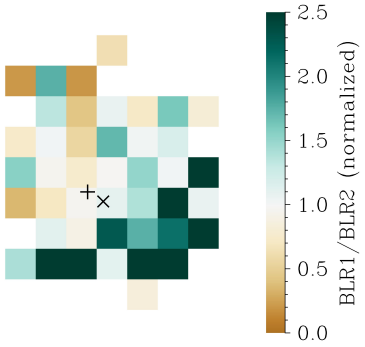

Fig. C.1. Ratio after peak flux normalisation of two BLRs from our mock sample. We plot pixels with $S/N \geq 0.5$. A NE to SW modulation is visible, as expected for the images of two point sources spatially separated along that axis.

Appendix E: Flux and kinematic maps of [O III]

In Fig. E.1 we show maps of the (narrow) [O III]$_{5007}$ flux, observed velocity and observed velocity dispersion, obtained from our spaxel-by-spaxel fitting described in Sect. 3.1. We observe a fairly smooth velocity gradient of about $\Delta v_{\rm obs} \sim 100$ km/s in ENE-WSW direction. In the NW region of J0148-4214, we find indication for a change in velocities, as well as an increase in velocity dispersion from the galaxy centre towards AGN III. This could support the notion that BH$_3$ is in the process of either being accreted onto J0148-4214 in a minor merger event or being ejected from J0148-4214 as a consequence of a previous black hole merger, i.e. in a recoil event where some of the gaseous material bound to the black hole is dragged along. However, we caution that the [O III] S/N in these outer regions is fairly low, and we thus prefer not to draw strong conclusions regarding the nature of AGN III based on these kinematic features.

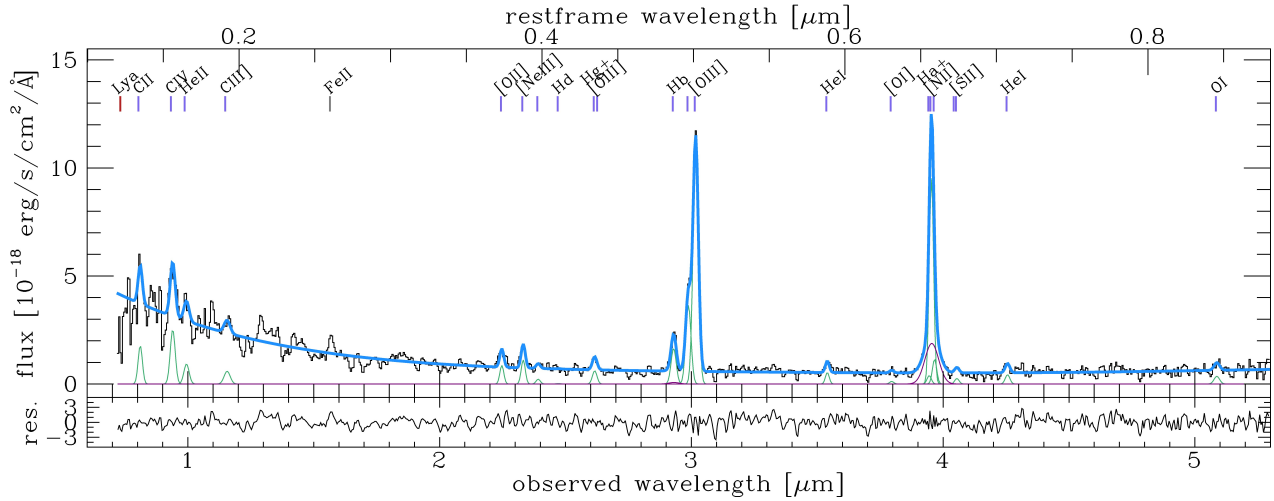

Fig. D.1. Fit to the prism spectrum extracted from the main galaxy (orange aperture in Fig. 1). The best fit is shown in blue, while the narrow and BLR components are shown in green and purple, respectively. Due to the lower resolution of the prism, the two-component structure of the Hα BLR seen in the high-resolution data cannot be resolved. We indicate the prominent emission lines. Lyα is not significantly detected. We indicate Fe II$_{2599}$ coinciding with possible emission excess at the corresponding wavelength.

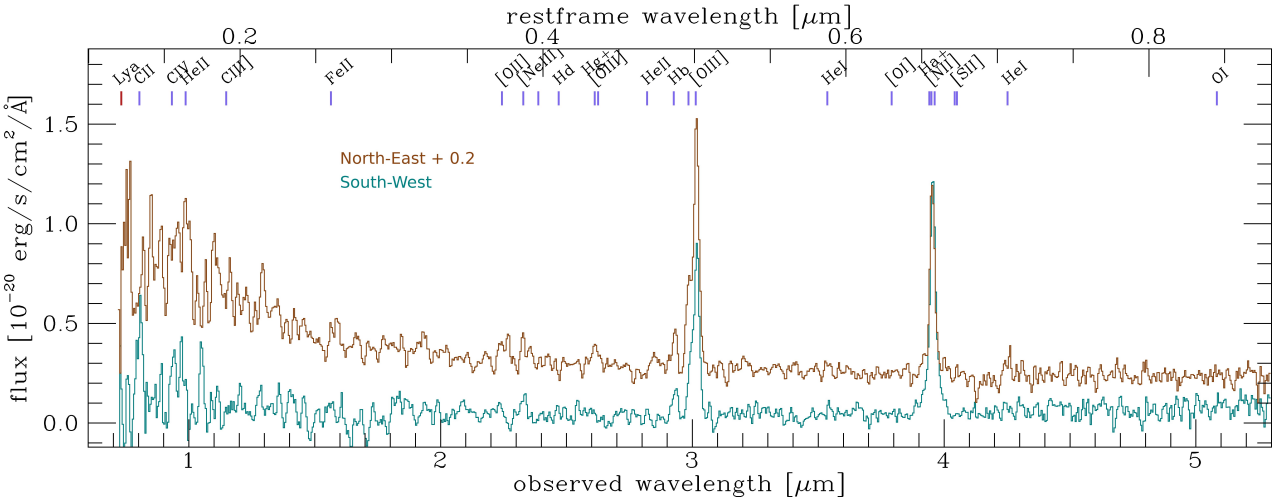

Fig. D.2. Two-by-two spaxel extractions from regions north-east (brown) and south-west (teal) of the centre of J0148-4214, highlighting the different blue continuum slopes and rest-frame optical strong line ratios. These differences could be due to different excitation sources, such as the two central black holes, or could be related to the small blue source seen close to J0148-4214 in the NIRCam imaging.

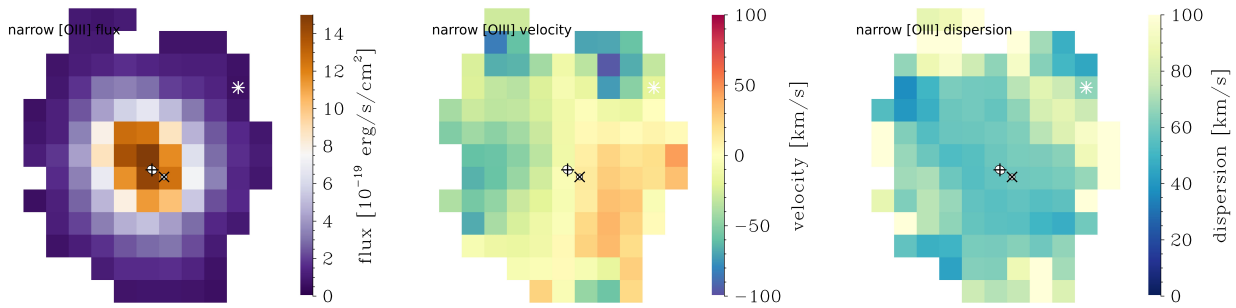

Fig. E.1. Maps of the [O III] flux, velocity, and velocity dispersion. We mark the positions of the three black holes as a cross (AGN I), plus (AGN II), and star (AGN III). We observe a smooth velocity gradient of about $\Delta v_{\rm obs} \sim 100$ km/s in the ENE-WSW direction (uncorrected for the PSF and inclination), and relatively constant velocity dispersion (corrected for instrumental resolution) throughout the main part of J0148-4214.